Flow Structure and Mixing Near a Small River Plume Front: Winyah Bay, SC, USA

Christopher Papageorgiou¹, George Voulgaris¹, Alexander Yankovsky¹ and Diane B. Fribance²

¹ School of the Earth, Ocean and Environment, University of South Carolina, Columbia SC, USA

² Department of Marine Science, Coastal Carolina University, Conway SC, USA

Correspondence to: George Voulgaris (gvoulgaris@geol.sc.edu)

Abstract. This study presents Eulerian data collected during the passage of a tidal plume from Winyah Bay, SC, USA. The data captured the evolution and structure of the plume and included high-resolution velocity and temperature time series, supplemented by T-S profiles from a MicroCTD profiler. The observations identified a pre-existing plume extending to 4 meters, with a water density of 1,023.6 kg m⁻³, laying above denser ambient waters. Upon arrival, the newly discharged tidal plume introduced a fresher layer (1,020.7 kg m⁻³) extending to 2.6 meters, gradually thinning due to radial spreading. The plume's frontal propagation measured at 0.36 m s⁻¹ with a calculated Froude number of 1.32, indicating gravity current dynamics. In the across-front direction a return flow was developed under the plume that extended throughout the water column, resembling an estuarine-like circulation pattern. This was associated with a vertical flow divergence, something not previously observed. Mixing processes were examined using the available overturn potential energy (AOPE) in the water column as described in Smith (2020). The analysis showed that near the bed, bottom boundary layer turbulence is the main mixing mechanism both before and after the passage of the front. In the surface layer, before the arrival of the front, mixing is driven by wind-induced shear and overturning. Within the gravity current, despite the high turbulent kinetic energy dissipation rates in certain regions, shear-induced mixing was minimal. These findings were reflected in the density diffusivity estimates near the surface that varied from 10⁻⁶ m² s⁻¹ prior to the arrival of the front, increasing to 10⁻⁵ m² s⁻¹ very near the front and diminishing to 10⁻¹⁰ m² s⁻¹ within the plume despite the high velocity shear observed there. The development of the counterflow under the plume, and the limited mixing within the plume despite the high shear observed there, suggest that plume induced straining may play an important role for plumes like the one studied here.

1. Introduction

5

10

15

20

25

30

Freshwater tidal plumes are common features in coastal environments, where rivers discharge nutrient-rich freshwater into saltier ocean waters. A plume discharged during ebb tide behaves like a jet outflow as it enters the coastal ocean. In the absence of high winds and strong coastal currents it transitions into a buoyancy-driven surface current that expands under the action of gravity (i.e., gravity wave). Further offshore, and assuming there are no constraints on the flow, the plume will turn until in achieves geostrophic balance and will propagate as a Kelvin wave (Münchow and Garvine 1993a). Under realistic conditions, the geometry, structure, and dispersion paths of freshwater plumes depend on wind forcing, river discharge, coastal circulation (including tides), and bathymetry (Horner-Devine et al., 2015). Moderate upwelling-favorable winds drive the plume offshore, causing it to thin and stretch into filament-like shapes that can extend tens of kilometers (Li et al., 2003; Yankovsky et al., 2022). Conversely, under downwelling conditions, the plume is compressed against the coast, deepening as it is driven parallel to the

shoreline (Fong and Geyer, 2002). During their evolution tidal plumes exhibit distinct flow structures that resemble those found in gravity currents created in the laboratory by Britter and Simpson (1978). This was confirmed by Imberger (1983) and Luketina and Imberger (1987) who used field observations to develop a conceptual model showing the similarities between gravity currents and tidal plumes.

35

40

45

50

55

60

65

70

In the absence of strong wind forcing, radial lateral spreading plays a significant role in mixing and plume evolution. Spreading stretches the plume horizontally, leading to thinning and increased velocity, which intensifies shear at the base of the plume. This shear drives mixing, which incorporates denser ambient water into the plume through entrainment. Entrainment increases the density of the plume, causing it to deepen and reduce its buoyancy, which may subsequently decrease its lateral spreading rate and overall velocity as it transitions to subcritical flow (Hetland, 2010; MacDonald et al., 2007). Usually, the base of the plume experiences stratified-shear instabilities at the plume / ambient water interface, which may cause mixing between the two water bodies (Kilcher et al., 2012, MacDonald et al., 2007). The frontal region is the most energetic as it forms a convergence zone that extends several meters into the water column. The mixing and turbulence are intense (O'Donnell et al., 2008) and TKE dissipation rates are of the order of 10^{-4} to 10^{-3} m² s⁻³ diminishing exponentially to $10^{-7} - 10^{-6}$ behind the front (Orton and Jay, 2005; O'Donnell et al., 2008; Horner-Devine et al., 2013; Delatolas et al., 2023). Recently, Spicer et al. (2021) argued that bottom generated tidal mixing can be important, especially under the influence of large tidal currents, as is the case for the Connecticut River discharging into Long Island Sound. They demonstrated that frontal mixing contributed only 10% to the total mixing in that system, with the remaining 90% being a balance between interfacial and tidal mixing, depending on tides' strength and river buoyancy input. In another study, Whitney et al. (2024) showed that although tidal mixing in the Connecticut River plume is important, interfacial mixing is the largest contributor. Although both shear and convection have been recognized as potential mixing drivers in the ocean (Ivey et al., 2020), traditionally, plume studies have focused mainly on the effect of shear on mixing the water column. Tidal straining (de Boer et al, 2006; 2008) has also been identified as a mechanism promoting stratification in the coastal ocean even under high shear conditions; however, its applicability in tidal plumes has not been considered yet.

To date our improved understanding of coastal circulation is guided by numerical modeling exercises. Such numerical experiments rely on existing parameterizations of turbulence and mixing to define the density diffusivity (K_{ρ}) , a parameter that defines the rate with which fresh water is mixing with the ambient saltier water. It is usually expressed as:

$$K_{\rho} = \Gamma \varepsilon_{\kappa} / N^2 \tag{1}$$

where ε_k is the turbulence kinetic energy (TKE) dissipation rate, N is the buoyancy frequency $(N^2 = -g/\rho_0 \partial \rho(z)/\partial z)$, where g is gravitational acceleration, ρ is water density with the subscript o denoting ambient salty water) and Γ is the mixing efficiency parameter defined as the ratio of the dissipation rate (ε_p) of turbulence potential energy (TPE) over ε_k (Smith, 2020) commonly parameterized using the flux Richardson number (Ri_f):

$$\Gamma = \varepsilon_p / \varepsilon_k = Ri_f / (1 - Ri_f) \tag{2}$$

The parameter Γ represents the amount of turbulence kinetic energy expended for mixing the water column in coastal stratified systems, and it is used widely to model mixing and estimating buoyancy fluxes in quasi-steady shear flows. In the absence of a robust expression for Ri_f (e.g., Mater and Venayagamoorthy, 2014), it is usually assumed that $\Gamma \approx 0.22$ (Peters, 1999; Kay and

Jay, 2003; MacDonald and Geyer, 2004; Osborn, 1980); however, Scotti (2015) showed that for isotropic overturn this value is 2. Alternatively, Burchard and Hofmeister (2008) in their work on mixing and stratification in estuaries and coastal seas (applying Simpson's (1981) concept of potential energy anomaly ϕ) used a bulk mixing efficiency $\Gamma = 0.04$, while Simpson et al. (1990) used a value of 0.003.

75

80

85

90

The objectives of this study are three-fold: (i) to present high quality experimental data of flow structure, stratification and turbulence from a relatively new site in the SE US and as such to enrich the database on tidal plume dynamics data available to the community; (ii) to examine how plumes interact with the ambient coastal ocean and determine the modification, if any, of the ambient water flow structure; and (iii) to evaluate mixing mechanisms and the relation of TKE dissipation rates to density diffusivity within a gravity plume.

Our study engages with the broader theoretical and observational efforts to understand circulation and mixing in buoyant, stratified flows, building off prior work (e.g., Marmorino and Trump, 2020, O'Donnel et al., 2008, Spicer et al., 2022). We utilize advanced methodologies to investigate full water column flow and density structure in the vicinity of the Winyah Bay, SC (USA) tidal plume front, under light upwelling wind conditions. High-resolution Eulerian time series of flow, temperature, and turbulence structure, extending close to the sea surface, are analyzed alongside individual temperature-salinity (T-S) profiles. Dissipation rates (ϵ) are estimated using a combination of acoustic Doppler current profiler (ADCP)-based techniques (Zeiden et al., 2023) and Thorpe sorting approaches (Smith, 2020). These methods allow for precise characterization of turbulent signals, mixing processes, and hydrographic characteristics (temperature, salinity, and density) across the plume front. By integrating these state-of-the-art approaches, this study provides details on tidal plume kinematics and assesses mixing efficiencies with unprecedented detail.

2. Experimental Setup

2.1 Data Collection

95

Data collection took place outside the mouth of Winyah Bay, an estuary located in South Carolina, USA. It is 29 km long, extends over an area of 157 km² and receives water from a drainage area of 47,060 km². It is a microtidal system, subjected to semidiurnal tides with a mean tidal range of 1.4 m at the mouth which at its narrower point is 1.2 km wide and ~8.2 m deep (Kim and Voulgaris 2005). The data presented here were collected as part of a larger synoptic survey of the Winyah Bay plume that occurred on board the R/V *Savannah* during the period April 12 to 15, 2023. This includes time series of velocity and temperature profiles, accompanied by distinct CTD and turbulence structure profiles collected at a single site (TS2) located some 10 km off the mouth of the estuary (Fig. 1). The mean water depth was 11.5 m, and the bathymetry is relatively smooth (see Fig 1a). The site was selected with the aim of capturing the propagation of a newly discharged tidal plume as it entered the coastal ocean.

105

100

Two floating platforms were deployed on April 14, 2023, for a period of ~4 hours capturing data for ~2 hours before and after the passage of a plume front. One platform (RoboCat) was a small catamaran structure equipped with a downward looking 5 beam Nortek Signature 1000 Acoustic Doppler Current Profiler (AD2CP) capable of providing high frequency, high resolution time series of horizontal and vertical currents extending close to the sea surface. The four slanted beams (Broadband, BB mode)

were configured to collect data at 1 Hz over a burst (ensemble) of 8.53 min (i.e., 512 profiles per burst). Cell bin size and range were 0.25 m and 15 m, respectively, and the blanking distance was set to 0.2 m. The 5th beam (HR mode) was sampling simultaneously, recording along-beam, radial velocities at a frequency of 8 Hz resulting in 4,096 radial velocity profiles per ensemble; the HR mode was configured with blanking and bin cell sizes of 0.20 m and 0.04 m, respectively (i.e., 171 cells over a range of 7 m). The burst data collection was repeated every 9 min resulting in a gap of 0.47 min between successive ensembles. For both BB and HR modes, after accounting for AD2CP transducer submergence, the first bin was located at 0.55 m below the sea surface.

The second platform was equipped with a thermistor array (t-array) consisting of 10 fast responding temperature sensors (RBR Coda3), arranged on a vertical aluminum rod. The rod was cantilevered from the platform and the individual sensors were separated by ~ 0.3 m. The array provided time series of temperature in the range extending from 0.02 m to 2.70 m below the sea surface with a sampling frequency of 2 Hz. The data were recorded using a specially built raspberry Pi microcontroller, equipped with a 12 port USB hub providing connections for the RBR units and a GPS unit (for time synchronization).

In addition to the platform, discrete CTD profiles and turbulence dissipation rates were acquired using an uprising MicroCTD profiler (Rockland Scientific) that was manually deployed from a small inflatable boat in the vicinity of the two surface platforms described above. A total of 16 individual profiles were collected at irregular intervals but overall distributed into periods before, during and after the front arrival. The exact timing of the profiles and their grouping in relation to the tidal plume front are discussed later in the results section (see Fig 3).

In-situ meteorological data (i.e., wind speed and direction, air temperature, barometric pressure, and relative humidity) were obtained from the meteorological station aboard the R/V *Savannah*. The data were recorded at a rate of 1 sample every 30 seconds. Surface wind stress is estimated using the Coupled Ocean-Atmosphere Response Experiment (COARE) algorithm version 3.6 (COARE 3.6, Fairall et al. 2003, Edson et al. 2013). The inputs to the algorithm included the recorded wind speed and direction, after they were averaged over periods of 512 s to match the AD2CP ensemble averaging scheme, and ship collected information of air and sea temperature, relative humidity, and barometric pressure. A downward IR flux of 400W/m² and a maximum daytime solar radiation of 900 W/m² were assumed. It should be noted that during data collection the vessel was in proximity to the site but stationed farther away (> 150 m) from the AD2CP and thermistor array, so as not to interfere with the flow in the deployment site.

Although no direct observations of the spatial extent of the plume exist, a Sentinel image (see Fig. 1b) obtained on April 15, 2023, at 15:49:31 UTC, ~2 hours after ebb provides a glimpse of the plume geometry. The imagery time corresponds to a similar tidal stage as that experienced during data collection and under similar wind forcing. The freshwater plume and associated front are clearly shown to be radially dispersing and at the time of the imagery its dimensions were ~ 11 x 7 km. The area of the plume

 (A_p) was estimated to be approximately 62 km².are clearly shown to be radially dispersing and at the time of the imagery its dimensions were ~ 11 x 7 km. The area of the plume (A_p) was estimated to be approximately 62 km².

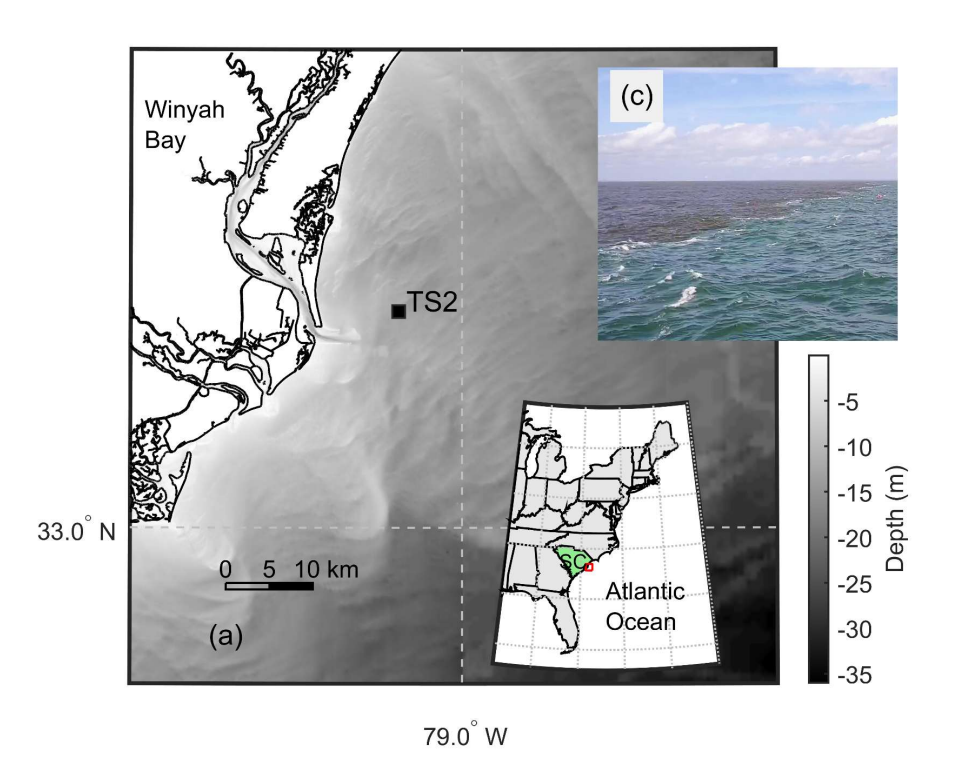




Figure 1: (a) Location of time series data collection (station TS2) off the coast of South Carolina, USA. (b) Sentinel L2 satellite image (modified Copernicus Sentinel data 2023 processed by Sentinel Hub) of a plume exiting Winyah Bay. Image was captured on 04/15/2023 at 15:49:31 UTC. The TS2 station location is also shown on the image while the coordinates shown are local with origin the mouth of the estuary. The across-front (u') and along-front (v') coordinate system used for current velocities us also show. (c) Photograph of the front examined in this study.

145 2.2 Turbulence Measurements

150

155

165

170

175

The Rockland Scientific microstructure profiler (MicroCTD) used was equipped with two piezoceramic shear probes, augmented by a fast thermistor, microconductivity sensor, and a JAC CT sensor for CTD measurements. The profiler was operated in an uprising mode providing raw data from approximately 9 m all the way to the sea surface. The CTD sampling frequency was 64 Hz corresponding to a vertical resolution of ~0.01 m and the temperature and conductivity measurements were synchronized using the actual uprising velocity and following the procedure recommended by the manufacturer. Discrete dissipation estimates from the MicroCTD deployments were obtained from the two perpendicular shear probes, using the Rockland Scientific provided processing tools (Lueck, 2016) with default cutoffs for spectral integration using the Nasmyth spectra vs. fitting to the inertial subrange at dissipation rates greater than 1.5x10⁻⁵ W kg⁻¹. Each spectrum was the average of individual spectra obtained from 1 s segments with 50% overlap. To maximize vertical resolution, each estimate represents a 2 s record (approximately 1.2 m), with 50% overlap between estimates. The FFT length for ensemble averaging within a spectral estimate was 1 s. The minimum depth for evaluation and minimum vertical velocity were 0 m and 0.5 m s⁻¹. Terminal speeds were approximately 0.6 m s⁻¹. Dissipation estimates corresponding to periods of high vibration were manually removed and the spectra from each shear probe were averaged prior to estimating a dissipation value.

In addition to the discrete dissipation profiles obtained with the MicroCTD, more regular dissipation profiles were estimated from the AD2CP HR radial velocity records using the structure function (SF) method (Wiles et al., 2006; Zippel et al., 2018; Scannel et al., 2017) following the process described in Zeiden et al. (2023). This method is suitable for use with moving platforms as it is immune to sensor motion (Thomson et al., 2019) and the second-order structure function (D) is defined as

$$D(z,r) = \langle (u_r'(z-r/2) - u_r'(z+r/2))^2 \rangle$$
(3)

where r is the spatial distance between measurements, <> denotes time averaging, and $u_r'(z)$ is the demeaned, instantaneous along-beam (radial) velocity. D is then related to the dissipation rate (ε) through the equation:

$$D(z,r) = C_v^2 \varepsilon(z)^{\frac{2}{3}} r^{\frac{2}{3}} + N(z)$$
(4)

where N is an offset representing the noise level in the measurements and Cv^2 (= 2.2) is a constant (Wiles et al. 2006). A least-squares linear regression of D(z, r) against $r^{2/3}$ at each elevation z below the sea surface is used to provide estimations of ε and N, with the latter being an indicator of the accuracy of the estimate.

The data were pre-processed following Zeiden et al. (2023) using their MATLAB® code. Pre-processing included removal of bad velocity values defined as those with low amplitude (< 40 dB) and/or low coherence (< 50). In addition, spikes in the data were removed using an along-beam median filter. Finally, wave bias was removed using an Empirical Orthogonal Function (EOF) based filter that removes profiles of wave orbital velocities estimated from the 4 larger EOFs. Following Zeiden et al (2023), in our analysis we used separation scales (*r*) ranging from one to four times the cell size (i.e., 0.04 m to 0.16 m). Additionally, in the post-processing flow, the resulting dissipation profiles were filtered based on a mean-square percent error (MSPE) of the least square fit of equation 4; only estimates with MSPE <5% were accepted. More details on the processing method can be found in Zeiden et al (2023).

It should be noted that a comparative analysis of dissipation estimates from the MicroCTD and AD2CP showed qualitative agreement (Papageorgiou, 2023, see Figs 2-28, 2-30 and 3.22 therein). The MicroCTD measurements are those from single profiles while the structure function estimates integrate data over a longer period (8.53 min), thus any variability shown in the microstructure data would not be visible in the SF method derived values. Overall, the estimates from both measurement systems display similar trends in the vertical and are of similar order of magnitude; and the variability observed in the profiles (with a maximum discrepancy of one order of magnitude) is likely attributed to the differing averaging periods. This assertion is further supported by the observation that the discrepancies between the MicroCTD and structure function estimates are comparable in magnitude to the variations observed among individual MicroCTD casts (Papageorgiou, 2023).

3. Results

180

185

190

3.1 Environmental Conditions

The Pee Dee average tidally corrected discharge during data collection was ~480 m³/s (USGS Station 02135200, located ~60km upstream the mouth of the estuary), which is above the average of 380 m³/s for this station. The Pee Dee River contributes ~55 to 60% of the fresh water discharged by Winyah Bay (Kim and Voulgaris, 2005) with the remainder being contributed by the Little Pee Dee (~20%) with contributions from the typical low discharge coastal plain rivers of Waccamaw (~8%), Black (~7%), Lynche (~7%), and Sampit (~1%) (Patchineelam, 1999, cited in Kim and Voulgaris 2005); these other rivers are not instrumented

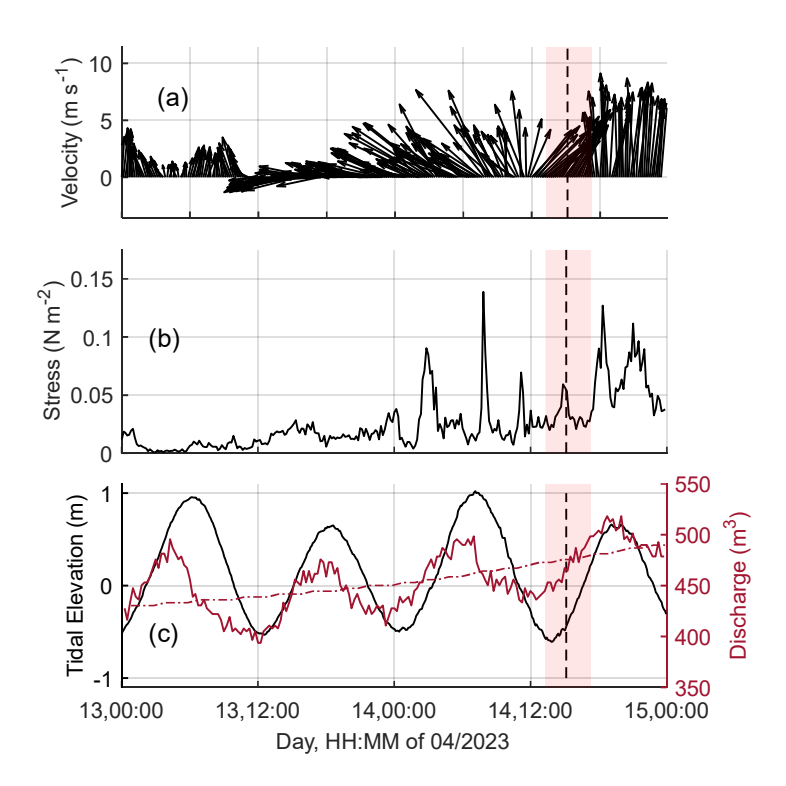


Figure 2: Time series of: (a) wind vectors for 2 days around the data collection period; (b) total wind stress estimated using the COARE 3.6 algorithm; and (c) measured tidal elevation (NOAA station 8661070) and recorded (solid line) and tidally corrected (dashed-dotted line) river discharge (USGS station 02135200). Vertical black dashed line represents the time of plume front arrival and the red shaded area denotes the data collection period.

and therefore the actual discharge from the mouth of the estuary is anticipated to be at least 1.5 times larger (i.e., ~720 m³/s) than that recorded at USGS station 02135200 (see Fig. 2b). Tidal surface elevation data (Fig. 2c) were available from NOAA station 8661070 (Springmaid Pier, SC) located ~56 km northeastward from the WB mouth. Data collection started at low water (LW) and proceeded up to ~2 hours before high water spanning the period LW to LW+4. During data collection winds were persistent toward the NE (upwelling favorable) with a mean wind speed and surface stress of 5.4 m/s and 0.031N/m², respectively (Fig. 2). The maximum wind stress observed during the sampling period was 0.053 N m⁻². at ~15:00 UTC. Wave conditions were calm to moderate with wave heights < 1.0 m and mean period ~7 s (NOAA NDBC Station 41024).

3.2 Near Surface Temperature Structure

195

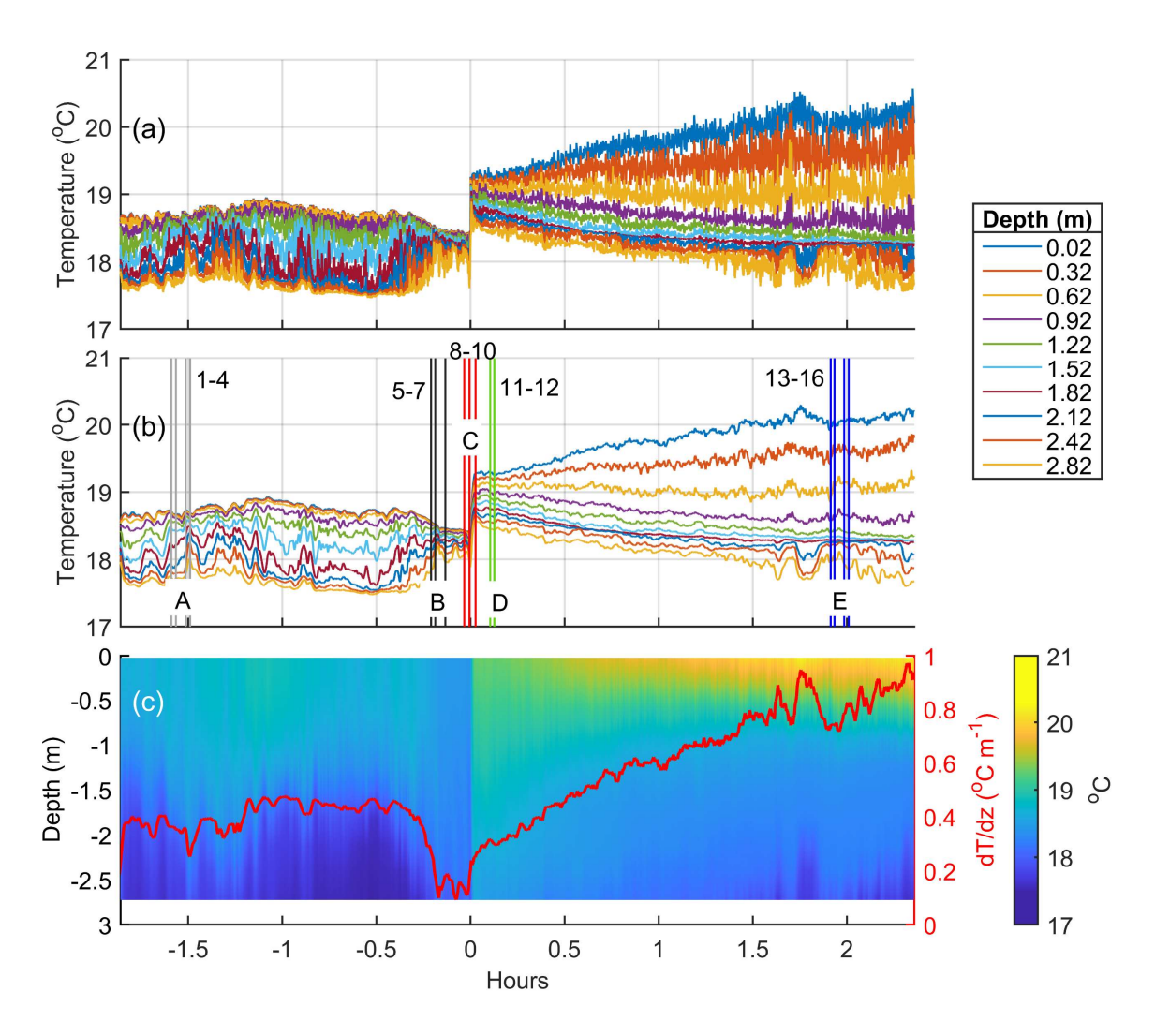


Figure 3: (a) Time series of the raw 2Hz recorded temperatures for each individual thermistor located at depths varying from 0.02 to 2.72m (see legend). (b) Same data as (a) but smoothed using a 180 point (90 s) moving average window. (c) Smoothed thermistor data (as in (b)) shown as a colored contour plot with temperature gradient (dT/dz) superimposed (red line). The vertical lines in (b) identify the times of MicroCTD data collection with the numbers adjacent to them denoting the cast number; the letters (A to E) represent the sorting of the casts into groups (see text for details). Times are relative to the time of plume front arrival.

The time series of both raw (at 2 Hz) and smoothed (using a 180-point (90 s) moving averaging window) thermistor array data are shown in Figs. 3a and b, respectively. The same smoothed data, gridded as a function of time and elevation, are displayed in the form of a contour map in Fig. 3c. Initially the near surface temperature ranged from 18.5 °C at the surface to 17.5 °C towards the bottom of the array (2.82 m below the sea surface). The arrival of the plume front (15:07 UTC time) is identified as the time when all temperatures from all depths collapse and shift to a higher temperature. This time corresponds to ~1.9 hours after LW. when the mean temperature over the top 3 m of the water column shifted from 18.3 to 18.7 °C,. The near-surface mean temperature gradient, defined as the difference between the bottom and top sensor temperatures, divided over their separation distance (2.82 m), was ~0.4 °C m⁻¹ until some 15 min prior to the arrival of the front. Then it dropped to 0.1 °C m⁻¹, increasing over time to almost 1.0 °C m⁻¹ toward the end of the data collection period, some 2.4 hours after the plume front passage (see Fig. 3c). As seen from the spacing of the 4 upper thermistor time series (Fig. 3b), the local vertical temperature gradient within the top 1 m of the water column increases from 0.1 °C m⁻¹ near the front to 1.4 °C m⁻¹ some 2 hours later.

It is worth noting the oscillations shown in the temperature record in water depths 1.82 to 2.42 m during the periods -1.6 to -1.0 hours. They have an amplitude of \sim 0.2 °C and are visible in both the raw and smoothed data. Similar oscillations are seen later in the record after the plume front has passed though (see times 1.5 to 2 hours). These latter oscillations are limited to the lowest three sensors corresponding to depths > 2m and indicate potential internal wave activity.

3.3 Temperature – Salinity - Density Profiles

205

210

215

220

225

230

The 16 MicroCTD profiles of temperature and salinity collected during this study were used to estimate water density utilizing the TEOS-10 (Thermodynamic Equation of Seawater, 2010) model. The time of each profile in relation to the front arrival is shown in Fig. 3b. Based on cast time, in relation to the time the front passed over the sensors, the profiles were sorted into 5 distinct groups. Casts 1-4 (group A) represent conditions before (\sim 1.6 hours) the arrival of the front, when the plume's leading edge was at some distance from the data collection site, while casts 5 – 7 (group B) represent conditions just before (\sim 10 min) the plume's front passed over the sensors. Data from casts 8 –10 (group C) correspond to when the plume front was exactly over the station. After the front's passage, casts 11-12 (group D), provide an insight of the conditions in the interior of the plume but near the front (some 5-6 minutes after). Finally, casts 13 – 16 (group E), provide the structure of water properties from the interior of the newly arrived plume well after (\sim 2 hours) the front had gone by.

The raw MicroCTD data are shown in a T-S diagram (Fig. 4) with different colors for different groups. Three distinct water masses can be identified corresponding to: (i) ambient deep water, (ii) a slightly lighter water mass representing pre-existing water mass, presumably from the previous tidal cycle; and (iii) that of the newly arrived, warmer fresher plume. Each water mass is characterized by a certain range of T and S with these two parameters exhibiting an almost linear T-S relationship but with different slope.

The vertical extent and structure of these water masses are displayed in the individual profile plots of temperature, salinity, and derived density (Fig. 5) and for each group separately. Group A and B profiles exhibit a consistent single step structure, while group C profiles show a two-step pattern that appears to persist in the profiles corresponding to groups D and E. These patterns are present in both temperature and salinity, something not surprising given the linear relationship between T and S (see Fig 4).

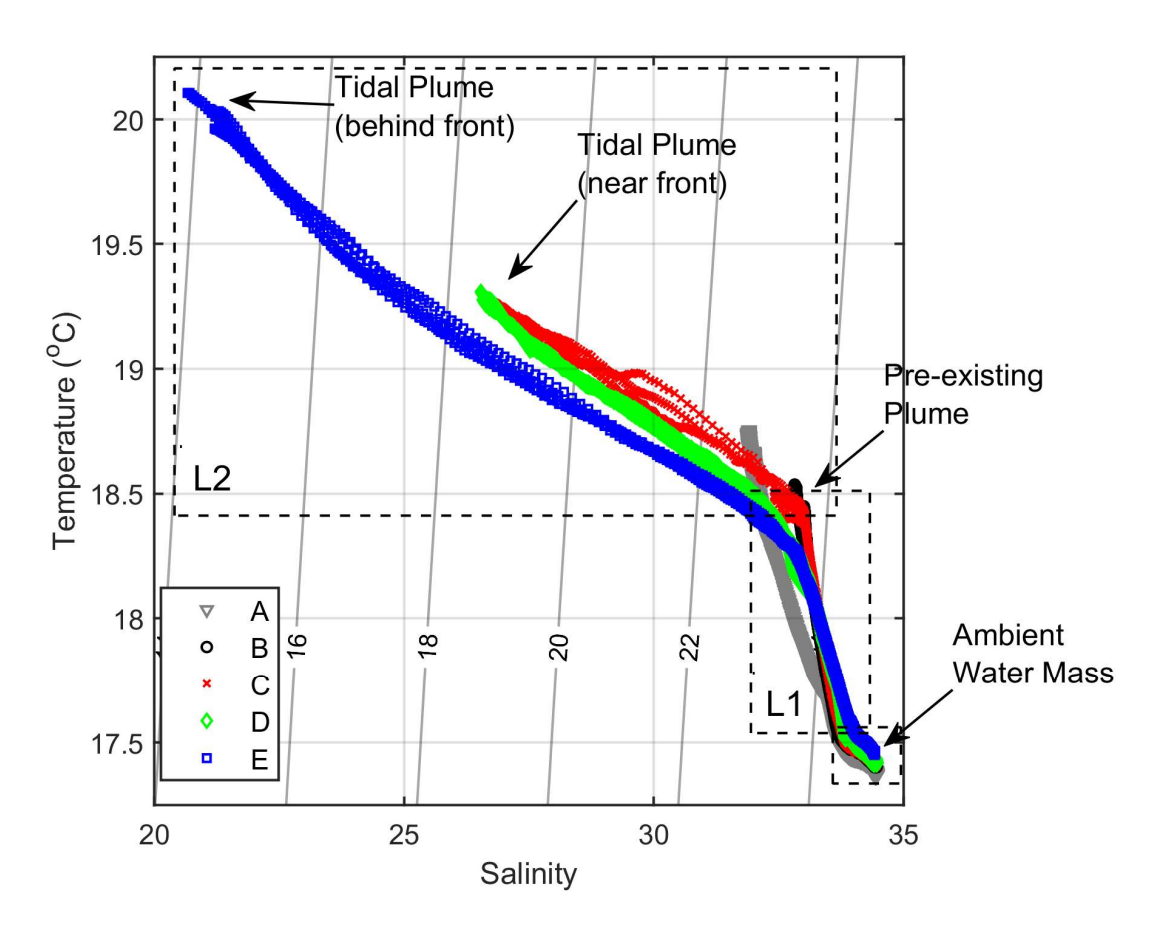


Figure 4: T-S diagram of the MicroCTD profile data collected during this study color-coded according to the group (A to E) they belong to (see text for details). The three dashed line boxes outline regions of the T-S space corresponding to the newly arrived layer (L2, top left), pre-existing (L1, middle box), and ambient (bottom right) water masses. End-members are indicated with arrows.

Initially, in Group A and B the uppermost layer (<2 m) displays temperature, salinity, and density levels of approximately 18.7 °C, 32, and 1,023 kg m⁻³, respectively. Meanwhile, the ambient bottom layer conditions (>6 m) remain relatively stable, with temperature ~17.3 °C, salinity 34.4, and density 1,024.8 kg m⁻³. This is also clearly delineated in the T-S diagram shown in Fig, 4. As the front passes through, a sudden rise in surface temperature is observed by approximately 0.7 °C; the water temperature kept increasing with time until the end of data collection (a total of 1.5 °C increase over a period of ~ 2 hours). A similar abrupt shift toward lower values is seen in salinity. At the time of the front's arrival (Group C) salinity reduces by approximately 5, eventually reaching a decrease of 12. In terms of density, the arrival of the front is associated with a decrease of 4 kg m⁻³, reaching densities of 1,019 kg m⁻³ near the sea surface (<2 m). In the interior of the plume (Groups D and E) fresh, lighter water was recorded with surface water densities close to 1,014 kg m⁻³.

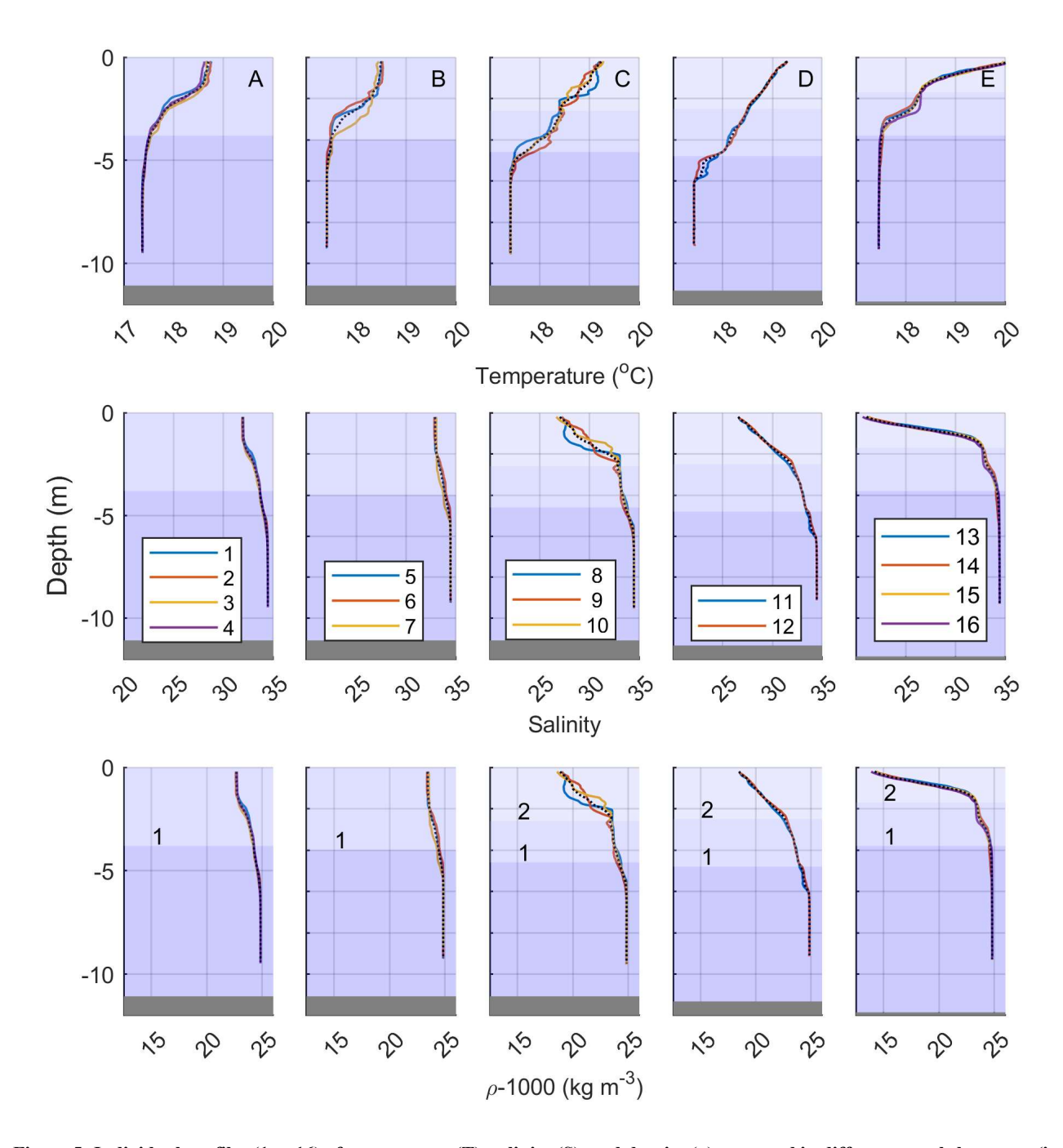


Figure 5: Individual profiles (1 to 16) of temperature (T), salinity (S), and density (ρ) arranged in different panels by group (i.e., 5 columns for groups A to E). Profiles within each group correspond to different location / distance from the plume front (see Fig. 3b). Black dashed lines indicate averaged profiles for each group. Different shades of blue, from darker to lighter represent the different water masses: ambient, pre-existing plume (layer 1), and new plume (layer 2), respectively. For the depths of each layer see discussion in section 4.

245 3.4 Flow Structure

250

During the ~4 hours of data collection, a total of 27 averaged velocity profiles (ensembles) were collected using the AD2CP. The east (u) and north (v) components of the flow were rotated to local across- (u') and along-front (v') components (i.e., u' is along the direction of front propagation and v' transverse to the front propagation direction, see Fig. 1c). The coordinate system for this rotation was determined from drone imagery (see Fig 12 in section 4.3) with the direction of the cross-front (u') component established as 50 °N. The vertical structure of the across- (u') and along-front (v') components is presented in Fig. 6a,b, in the

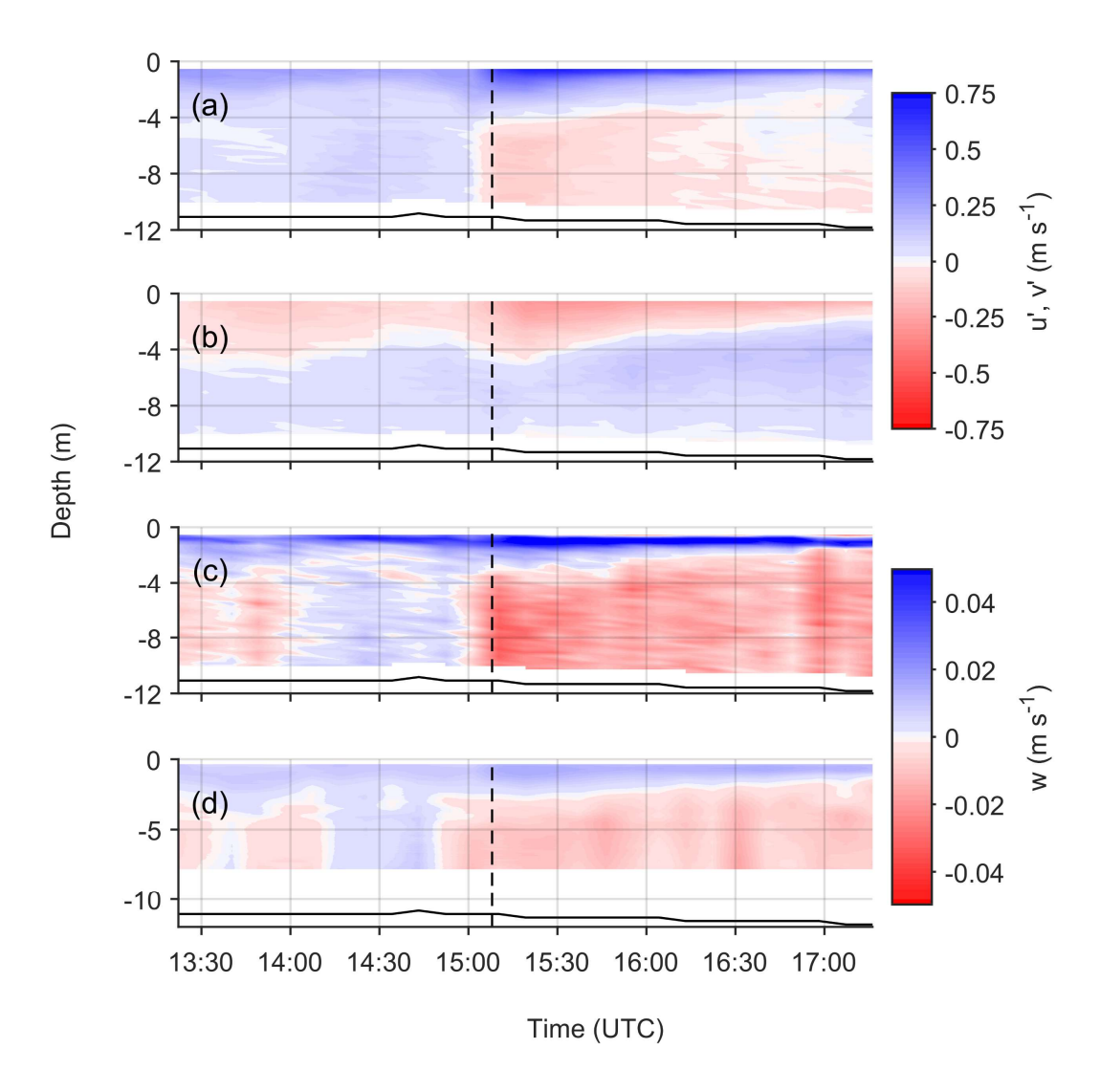


Figure 6: Vertical and temporal distribution of averaged current velocity components: (a) cross-front velocity component, u' (i.e., in the front propagation direction), (b) along-front velocity component, v', positive toward the coast (i.e., transverse to the front propagation direction), (c) vertical (w) component from the 4 beams BB data, and (d) vertical (w) component from the 5th beam. Data in (a), (b) and (c) represents an 8.53-minute average while in (d) the average is 4.27 minutes. Vertical dashed line indicates the time of front arrival; the depth is shown as a solid black line. Note the different velocity scales for the horizontal and vertical velocities.

form of contour plots. The vertical dashed line in Fig 6 indicates the time of the front arrival as has been determined from the temperature profiles shown in Fig. 3.

In the along-front propagation direction (Fig 6a), before the arrival of the front, the u' component is uniformly positive throughout the water column with a depth averaged value of \sim 0.10 m s⁻¹. With the front's arrival, the upper layer averaged flow intensifies to \sim 0.28 m s⁻¹ and then diminishes over time to \sim 0.07 m s⁻¹, toward the end of the data collection period. During this time, a return flow develops under the surface layer with a vertically averaged (within the return layer) velocity that ranges from approximately -0.10 m s⁻¹ immediately after the arrival of the front to -0.02 m s⁻¹ toward the end of the data collection period. The observed flow pattern resembles that of estuarine circulation, and it is clearly associated with the arrival of the new plume. Estimates of the vertically (by layer) and temporarily (from the time to the front arrival to end) integrated velocities indicate upper- and lower-layer velocities of 0.174 m s⁻¹ and -0.044 m s⁻¹, respectively. Multiplying by the respective average depth layers of \sim 2.5 m and \sim 9.0 m we get fluxes of 0.43 and 0.39 m³ s⁻¹ per m width, a difference of \sim 10% from their mean value.

255

260

265

270

The along-front flow component v' (Fig 6b) shows a pattern of offshore (negative) flow near the surface and onshore directed flow below. This pattern is consistent before and after the arrival of the front with the flows being slightly intensified during the latter period. The mean velocities of the offshore directed upper layer are \sim -0.05 m s⁻¹ and \sim -0.07 m s⁻¹ before and after the front arrival while those of the onshore (positive) directed bottom layer are \sim 0.06 m s⁻¹ before the front arrival, doubling to \sim 0.13 m s⁻¹ after that time. The increase in velocity at this time could be due to errors in defining the along-/across-front coordinate system, due to undulation of the front as it is not linear (see Fig 1c), or due to tidal influence.

In the along front propagation direction (u'>0) the plume (surface layer) exhibits a shallowing over time (Fig. 6a) with its base starting at \sim -4 m when the front arrives and linearly shifting to \sim -2 m at the end of the data collection period. This is likely due to radial expansion, but it can also be related to the formation of the trailing front, as described in a semi-analytical model of a radial supercritical plume forced by a constant discharge (Garvine, 1984). This shallowing over time suggests that for particular depth levels (changing over time) a gradient du'/dt <0 is present implying an across-front flow convergence (du/dx<0, assuming dx=U*dt, with U being an appropriate velocity scale associated with the tidal plume). Continuity arguments suggest that such convergence should drive vertical currents something shown in Figs 6c and d.

Two values of vertical velocity are available: (i) a value estimated from combining the 4 slanted BB beam radial velocities (Fig. 6c), and (ii) from the 5th beam radial velocity (Fig. 6d). Both vertical velocity estimates agree qualitatively, although the BB velocities show slightly higher values. The 5th beam radial velocities are considered more accurate as they do not suffer from the potential of contamination from the horizontal velocities due to tilt errors. Both records show a consistently positive (upward) flow close to the sea surface (<2 m) for the whole period of data collection. Farther below just before and after the front's arrival negative velocities are seen, of the order of 0.02 m/s (Fig 6d) and persist all the way to the seabed. The depth of the divergence (dw/dz<0) appears to correlate to the depth-varying divergence in the across-front velocity (Fig 6a) discussed earlier.

3.5 Acoustic Backscatter

285

290

295

Acoustic returns include scattering by both turbulent salinity microstructure and particles in suspension (Lavey et al, 2013). Our AD2CP data lack sound spectral characteristics to allow for separation of the different backscattering sources. Furthermore, the acoustic frequency of 1 MHz falls in the region where both salinity microstructure and fine sediment-induced backscatter are equally important (see Fig. 2 in Lavey et al., 2013). Despite these limitations, acoustic backscatter data provide qualitative information describing the conditions during the data collection period. Fig 7 shows a time series of the intensity of the return acoustic signal (16 s averages) from both the HR 5th beam (Fig. 7a, vertical resolution 0.04 m, sampling frequency 8 Hz) and transducer 1 of the broadband (BB) array of the sensor (Fig. 7b, vertical resolution 0.25 m, sampling frequency 1 Hz). The HR return (Fig. 7a) does not extend to the seabed while the BB transducer 1 (Fig. 7b) data does. Both data sets were corrected for geometric spreading and attenuation due to water absorption. Three major patterns are evident: (1) very high acoustic intensity at the time of the arrival of the front, presumably to particulates and detritus accumulated in the front convergence zone; (2) increased acoustic backscatter near the sea bed that is confined at depths >6 m prior to the arrival of the plume and then after the front arrival expanding to shallower depths (~4 m), especially toward the end of the time series; (3) increased intensity near the sea surface after the arrival of the plume that expands to deeper depths over time. The patterns described in (2) and (3) lead to the development of a lower backscatter region in mid-waters with a vertical extent that reduces over time after the arrival of the plume, suggesting a merging of the top and bottom high backscatter layers. In the region of lower backscatter intensity, prior to the arrival of the plume, we see evidence of internal waves (IW) with periods varying between 5 and 9 minutes. These IWs

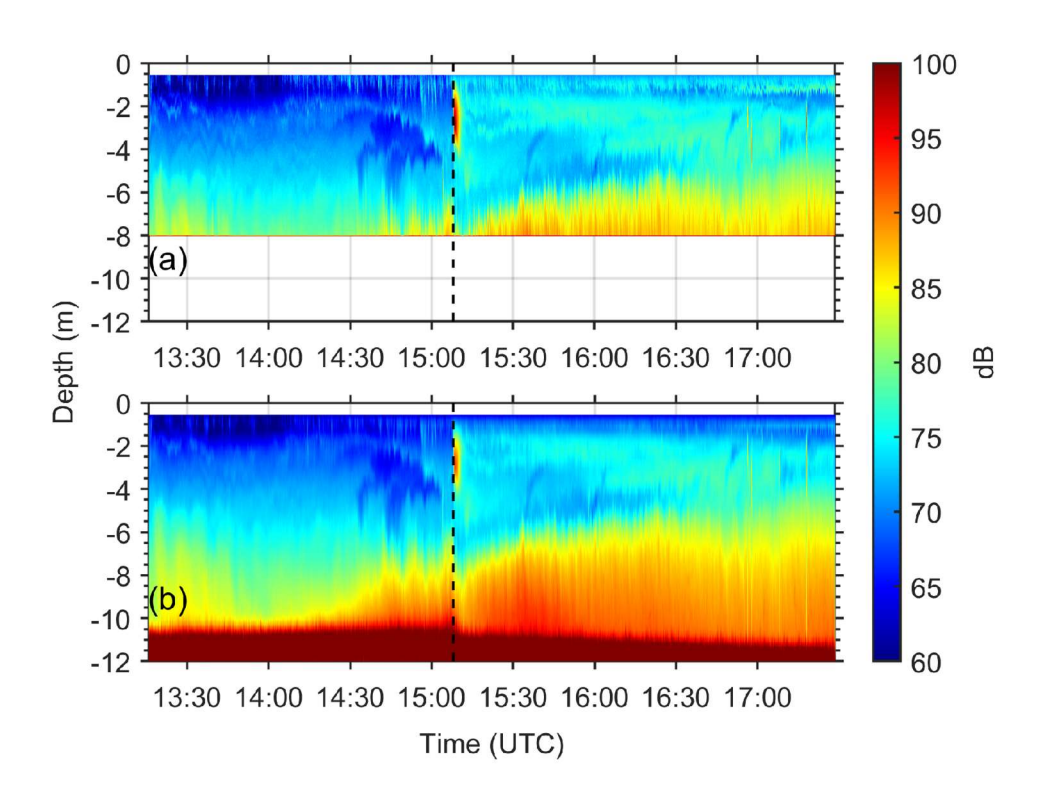


Figure 7: Time series of acoustic backscatter profiles corrected for geometric spreading and water attenuation. (a) From the HR 5^{th} beam record with a vertical resolution of 4cm, extending to \sim 7.5 m depth; (b) from one of the Broad Band transducers (beam 1) extending all the way to the sea bed (vertical resolution 25cm). Both records are 16 sec averages of individual pings collected at 8 Hz and 1 Hz for the HR and BB transducers, respectively.

correspond to the times and depths (~2 m) of the IWs identified in the lower sensors of the thermistor array (see Fig. 3b). No clear evidence is present for the period after the arrival of the front suggesting minimal, if any, role of flow instabilities in mixing processes.

3.6 Tidal Dynamics

300

305

310

The short record length (~4 hours) of the time series shown in Fig. 6 does not allow resolution of the tidal signal using harmonic analysis. Instead, the mean velocities from a total of 80 ensembles from 64 stations occupied during the study period aree utilized. These stations are in the general area of the sampling site (see Fig 8 bottom left) and the data were collected at different times over a period of ~5 tidal cycles from April 12 to April 15, 2023. The assumption made here is that the spatial variability of the tidal signal in the area is not significant. Only depth-averaged velocity data from water depths > 4.5 m are used in the analysis to ensure that the tidal current estimates are not influenced by plume-associated flows. This depth was defined based on the CTD profiles (see Fig 5) and experiments using small variations in the selection of depth did not show significant changes in the results. The harmonic analysis was carried out for the two horizontal flow components using only periods corresponding to the semi-diurnal (M2) and diurnal (O1) constituents. Resolution of more semi-diurnal (i.e., S2 etc.) or diurnal constituents is not possible due to the length of the time series and all energy from adjacent frequencies are included in the two components used

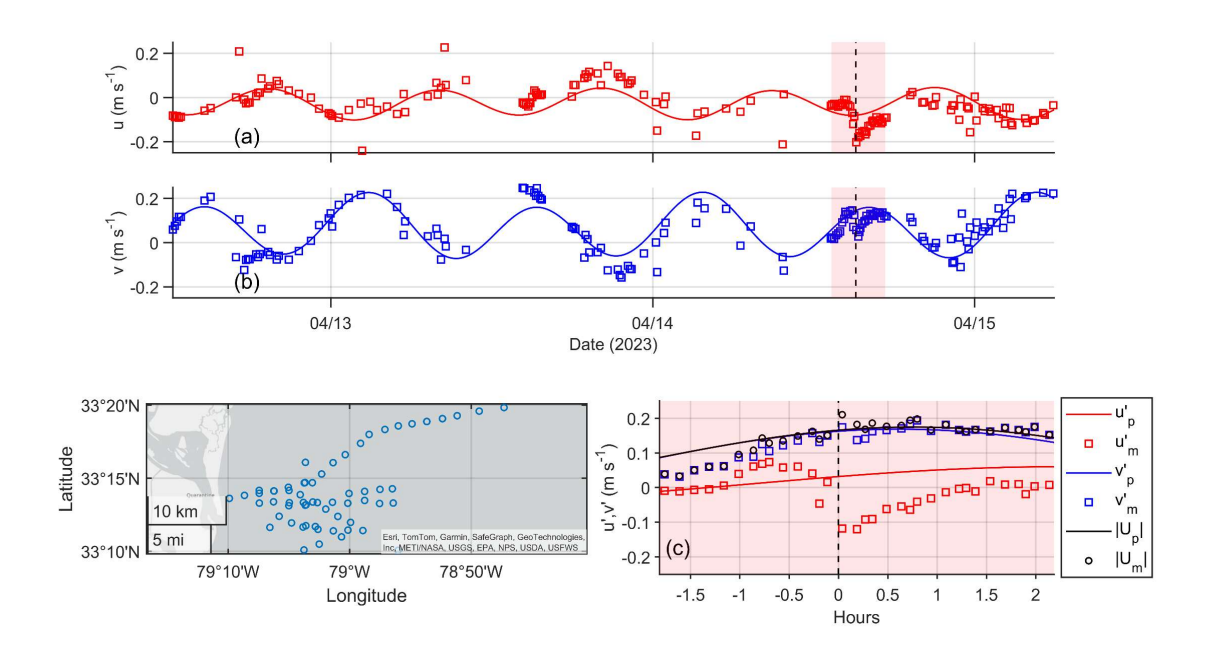


Figure 8: Time series of (a) east (u) and (b) north (v) bottom averaged (depths > 4.5 m) velocity components from all stations occupied during the period April 12 - 15, 2023; map in bottom left shows the station spatial distribution. The reconstructed tidal flow is shown as solid line and it was developed using the results of the harmonic analysis. The shaded area indicates the period station TS2 was occupied. (c) Close up of the measured and predicted tidal flows with the time in hours relative to the time of plume front arrival rotated in across-front (u') and along-front (v') components; subscripts m and p denote measured and predicted flows, respectively.

in the analysis. In Fig. 8a and b the reconstructed time series of the tidal flows are shown together with the velocity data used as input in the least-square analysis.

The M2 and O1 amplitudes estimated were 0.08 and 0.01 m s⁻¹ for the east (u) component and 0.01 and 0.03 m s⁻¹ for the north (v) component of the flow. The corresponding relative phases were 215.1 and 73.8 degrees for u and 67.5 and 251.5 degrees for v. The overall mean tidal flow values were -0.01 and 0.07 m s⁻¹ for u and v, respectively.

In Fig 8c the predicted tidal flows and measured velocities are shown in across- (u') and along-front (v') coordinates. The along-front component (v') seems to follow the tidally predicted component, for most of the time. On the other hand, the across-front component (u') shows the largest deviation from the predicted tidal velocity in response to the tidal plume. The largest deviation occurs at the time of the front arrival (negative return flows) and diminishes over time. This confirms that although the along-front flow (v') is predominantly tidal, the cross-front component (u') is mainly the result of the arrival of the plume.

3.7 Turbulence Dissipation

320

330

335

340

345

Figure 9a shows turbulent kinetic energy (TKE) dissipation rate (ϵ_k) profiles estimated from the AD2CP vertical beam radial velocities using the second-order structure function (SF) method (see section 2.2). The gaps seen in the profiles at mid-water levels are because of interference between two successive pulses and are a result of the shallow operating depth of the AD2CP. These data failed the MSPE (<5%) error criterion, as did some other data as shown in the figure.

Prior to the front's passage, dissipation rates near the surface (< 2 m) are relatively high, of the order of 10^{-5} m² s⁻³ and decrease with depth down to 4 m. At greater depths (> 4 m) dissipation rates remain relatively constant and $< 10^{-8}$ m² s⁻³. After the front's passage, the dissipation rates exhibit a more complex structure, with high rates near the surface as expected, reducing to 10^{-7} m² s⁻³ at greater depth and then increasing again (secondary peak) before decreasing again toward the 4 m depth. The secondary peak appears as a band of elevated TKE dissipation rates starting at $\sim 3 \text{ m}$ immediately after the passage of the front and reducing in depth with time reaching approximately 1 m about 2 hours after the front's arrival. In the lower water column (> 6 m) dissipation rates are lower before the arrival of the front than after. This is attributed to benthic boundary layer processes and increased near bed total current speeds mainly because of the tides (see Fig. 8c).

Although vertical velocities from the 5th beam were presented in Fig. 6d, the same data after correction for wave bias using the EOF method described in Zeiden et al. (2023) are shown in Fig. 9b. They do show the same pattern as that of the raw velocities, i.e., persistent positive (upward) flow close to the surface and predominantly negative (downward) flows at greater depths after the passage of the front, but the velocity magnitudes are smaller by a factor of ~ 2, never exceeding 0.02 m s⁻¹ As in Fig. 6, a clear divergence in vertical flow is evident that starts at ~ 3.5 m depth just behind the front that linearly moves to shallower depths over time (see dashed line in Fig 9b). As discussed earlier, this area of divergence seems to be associated with regions of across-front velocity convergence and appears to coincide with both the depths of elevated dissipation in the upper water column seen in Fig. 9a and with the region on relatively higher velocity shear (S) levels shown in Fig. 9c. It is worth nothing that the latter correlation is more with the base of the higher shear layer (bottom of tidal plume) and not necessarily with the highest shear levels that are found mainly close to the surface (Fig. 9c).

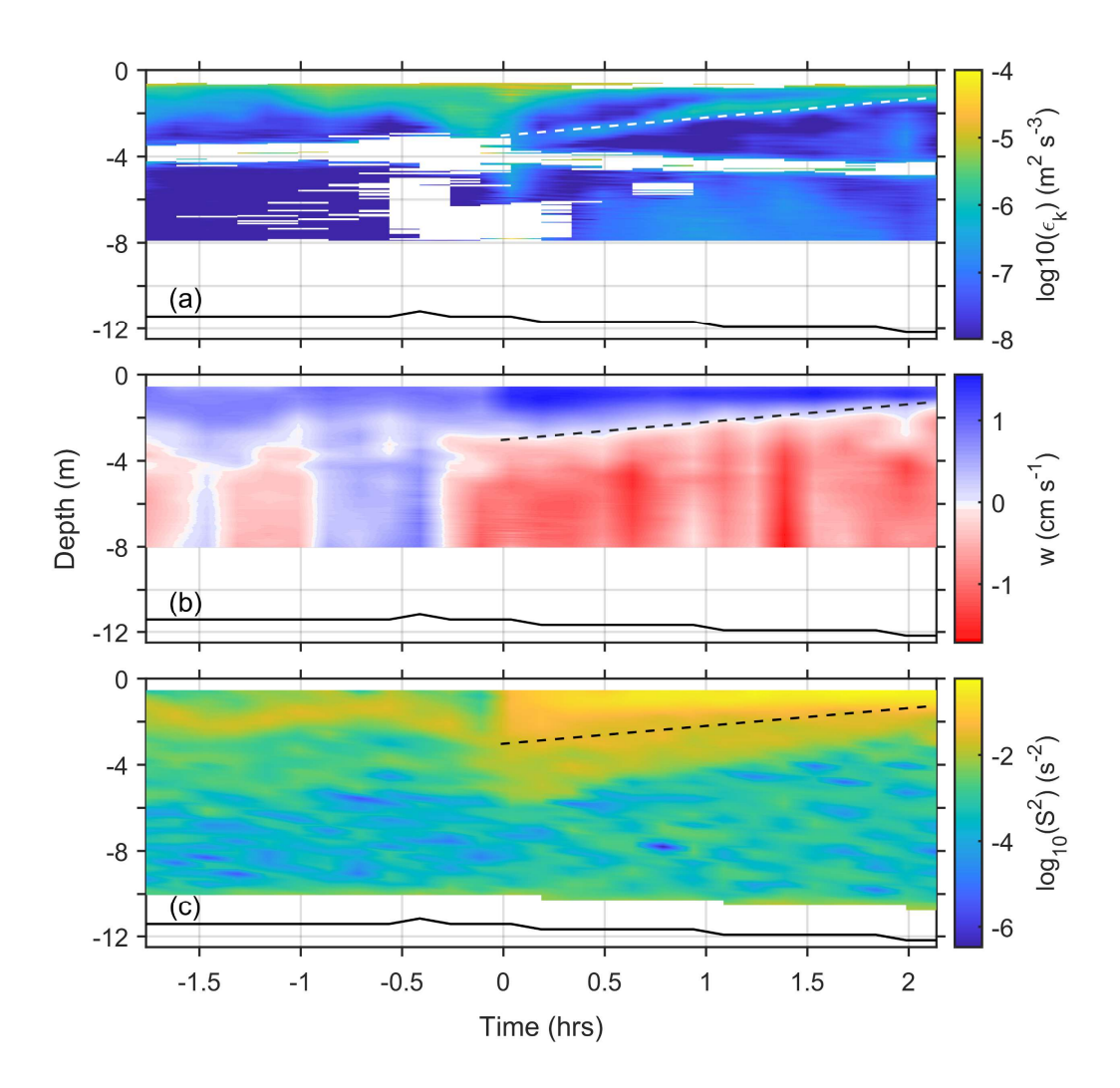


Figure 9: Time series of vertical distribution of: (a) Dissipation rate (ϵ_k) estimated from the AD2CP 5th beam HR radial velocity profile using the structure function (SF) method (see section 2.2). The plot is created using 27 individual profiles corresponding to each one of the AD2CP 4.27 min ensemble. (b) Mean vertical velocity estimated after waves were removed using an EOF method (Zeiden et al., 2023). (c) Log of the square velocity shear (S²) estimated from the horizontal velocity components shown in fig. 6. Dashed line is used to identify the location of vertical velocity divergence in all panels.

4. Data Synthesis and Discussion

4.1 Plume Structure

350 The T-S-density profile results presented in Fig. 5 reveal a water column that transitions from a single-step to a two-step density structure. This suggests the presence of a pre-existing plume (hereafter referred to as layer 1) from the previous tidal cycle followed by the arrival of a newly discharged tidal plume (layer 2) that propagates above it. The system transitions from a two-layer model (ambient waters and pre-existing fresher water mass) before the arrival of the front to a three-layer model afterward. Although various investigators have used a particular isohaline to delineate a plume (i.e., S=21 in Kastner et al., 2018, S=27 in

McDonald and Geyer, 2004 etc.) the T-S diagram shown in Fig. 4 suggests that the depth of the warmer tidal plume is defined by temperature and salinity values > 18.3 °C and < 32.7, respectively. This depth is 2.9 m initially reducing to 1.9 m toward the end of the data collection period. We quantitatively estimated the plume depth using the generalized equation of Arneborg et al. (2007), after modifying it for a three-layer structure (see Appendix A). The estimated depths for the pre-existing (D₁) and the new (D₂) plume are listed in Table 1 and provide each layer's vertical extend both before ($t < t_f$) and after ($t > t_f$) the front's arrival

Table 1: Depths of pre-existing (D₁) and newly arrived (D₂) plumes for the times corresponding to the different group profiles.

	$t \le t_f$		$t \approx t_f$	$t > t_f$	
Layer Depth	A	В	С	D	Е
D ₁ (m)	3.8	4.0	4.6	4.8	3.8
D ₂ (m)	0	0	2.6	2.5	1.7

Initially, the pre-existing plume (layer 1) has a depth (D_1) of 3.8 meters. The arrival of the newly discharged plume (layer 2) causes a depression in the interface between the pre-existing plume and the ambient waters by approximately 1 meter, though this depression gradually diminishes over time. Over the course of the experiment, the depth of the newly discharged plume

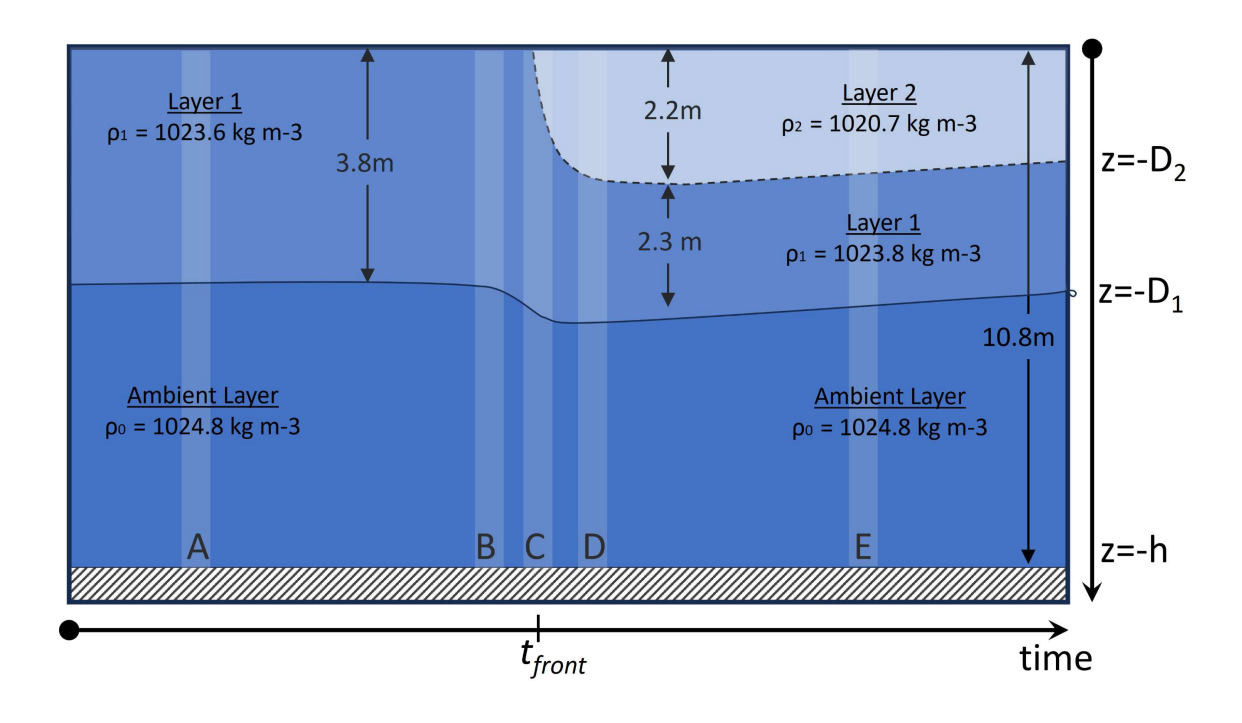


Figure 10: Conceptual model describing the structure of the water column throughout the data collection period. Initially a 2-layer structure is present $(t < t_f)$ where an upper layer of depth D₁ and density ρ_1 , presumably from a previous plume, is over ambient ocean waters with density ρ_0 . The front of a newly discharge tidal plume of depth D₂ and density ρ_2 arrives at $t = t_f$, contributing to the creation of a 3-layer structure. The vertical shaded bands denote the time / relative location of the microCTD profile groups shown in Figure 3b.

gradually decreased from 2.6 to 1.7 meters, indicating a reduction by a factor of 0.75 over a period of \sim 2 hours. The D_1 and D_2 depths presented above appear to correspond to the 34 and 32.5 isohalines, respectively.

Utilizing the depths in Table 1 and the density profiles shown in Fig. 5, the mean water density within each layer was estimated and a conceptual schematic of the water column during the experiment is constructed and shown in Fig. 9. The pre-existing plume maintained a depth close to 4 meters, with an average density of 1,023.8 kg m⁻³ (S = 33.1), overlying ambient ocean waters with a density of 1,024.8 kg m⁻³ (S = 34.3), while the new plume had an average density of 1020.7 kg m⁻³ (S = 29.3).

4.2 Frontal Propagation

370

375

380

385

390

The absolute speed of the front was estimated from the upper bin of the AD2CP that was located at 0.55 m below the sea surface (Fig. 11) and successive photographs collected from a drone (Fig. 12). Both methods revealed a frontal propagation toward the ENE with an absolute front speed of 0.61 m s⁻¹. Although the propagation of the front, as shown in the imagery (z= 0 m) is 50 °N, the direction of the mean current of the upper bin (z=0.55 m) of the AD2CP is 74 °N. The water mass behind the front was moving with absolute speeds of 0.72 and 0.75 m s⁻¹ some 8.5 and 17 min after the front passage, respectively. The layer-depth averaged velocities of the front and plume behind it, after subtracting the layer-averaged velocity of the layer underneath were 0.36 m s⁻¹ and 0.40 m s⁻¹, respectively, suggesting an overtaking velocity of 0.04 m s⁻¹. The vertically and time averaged across-(u') and along-front velocities (v') of the different layers identified in this study and schematically shown in Fig 10 are listed in Table 2.

Table 2. Vertically integrated and time averaged velocities (in cm/s) for each layer shown in Fig. 10 prior to $(t < t_f)$ and after $(t > t_f)$ the arrival of the front. Velocities shown are in the cross-/along-front coordinate system.

. cm/s	$t \le t_f$			$t > t_f$		
	u'	v'	U	u'	v'	U
Layer 2	-	-	-	27.54	-3.27	27.73
Layer 1	10.17	-0.95	10.21	1.55	16.32	16.39
Ambient	2.24	7.64	7.98	-2.73	15.87	16.11

respectively. Based on these values a frontal Froude number $(F_r = U_f/(g'D_2)^{1/2})$ of 1.32 is estimated. This value is between the theoretical value of 1.42 expected for a freely propagating gravity current (von Karman, 1940) and the value of 1.19 suggested by Huppert and Simpson (1980). The flow remained supercritical (Fr>1), although diminishing over time for 2 hours after the front passed over the station. Using an average water depth of 11.5 m and the frontal speed of 0.36 m/s a frontal Reynolds number ($Re_f = (U_f h)/v$) of 4.03 x 10⁶ is estimated, a value very similar to that found for the Merrimack River plume by Horner-Devine at al. (2013). The bulk-mixing coefficient (β , Simpson and Britter, 1979; 1980) was calculated to be 0.11 which is less

The reduced gravity g' and the mean depth of the layer of the plume (layer 2, D2) were found to be 0.034 m s⁻² and 2.2 m

than half of the value of 0.37 reported in Pritchard and Huntley (2002).

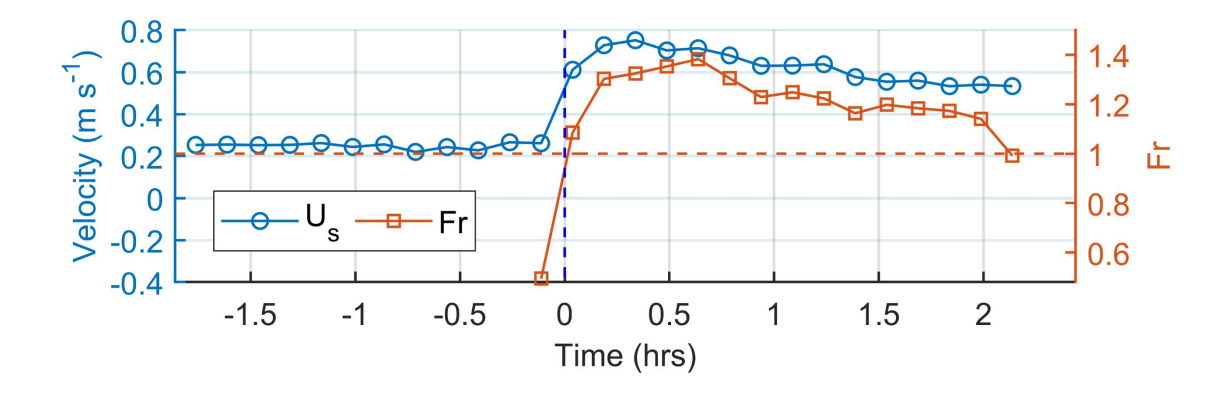


Figure 11: Near surface currents (U_s) before and after the arrival of the plume measured by the first bin of the AD2CP (z=0.55 m) and Froude number (Fr) variability inside the newly arrived plume.

Although there are no direct observations of the spatial structure and spreading rate of the plume, the Sentinel image collected the day after the experiment (see Fig. 1) provides a snapshot in time of the plume shape and areal extent at that time. As in Pritchard and Huntley (2006) assuming a semicircular shape, the area of the plume (Ap(t_f)=62 km²) was used to estimate the plume effective radius to be 4.4 km.. Using the observed plume velocity of 0.33 m s⁻¹ (1.2 km/h) as a representative value of a linear spreading rate (see Pritchard and Huntley, 2006), then the change of the effective radius variability during the time elapsed between the front's passage from the sensors to the end of the data collection period (~2 hours) is ~ 6.7 km. Assuming an instantaneous release of freshwater and conservation of mass, then the reduction of the plume depth over the 2 hours of observation is estimated to be ~ 0.43 m. This is an extreme value estimate assuming all river discharge occurred instantaneously at t LW and there was not a continuous supply of fresh water. The shallowing of the plume observed is of the order of 0.60 (using the density profiles in Fig 5) which is greater than the 0.43 value but reasonable given the uncertainties of these estimates.

4.3 Plume Flow Strurcture

395

400

405

410

415

As discussed in section 3.4 the flow structure along the direction of the plume propagation is characterized by the development of a return flow under the plume (Fig. 6a) resembling that of estuarine circulation. The strength of the return flow reduces over time as the plume spreads. Tidal analysis (Fig. 8c) clearly shows that the predicted tidal velocity component along this direction is weak (from 0 to 0.05 m/s), and the return flow deviates significantly from the expected tidal signal. Crude 2-D water mass conservation analysis (per unit width of water column) showed a closure within 10% supporting the argument of the development of a plume-driven return flow. Although opposing flows underneath tidal plumes have been described before (e.g., Horner-Devine et al., 2009) these represented ambient water conditions that the plume was discharged into. Shipborne flow observations on the Merrimack River by MacDonald et al. (2007) did not capture such return flows. In another study on the same area Spicer et al. (2022) observed return flows under the detached Merrimack River plume, but those were attributed to the tidal patterns of the area and not the plume itself. More recently, Delatolas et al (2023) using an AUV reported return flows that were thought to be associated with the front convergence zone reaching all the way to the sea bed; however, since the study was focusing on mixing and not flow structure, no evidence was presented to identify the role of tides as was the case in Spicer et al. (2022) for the same location.

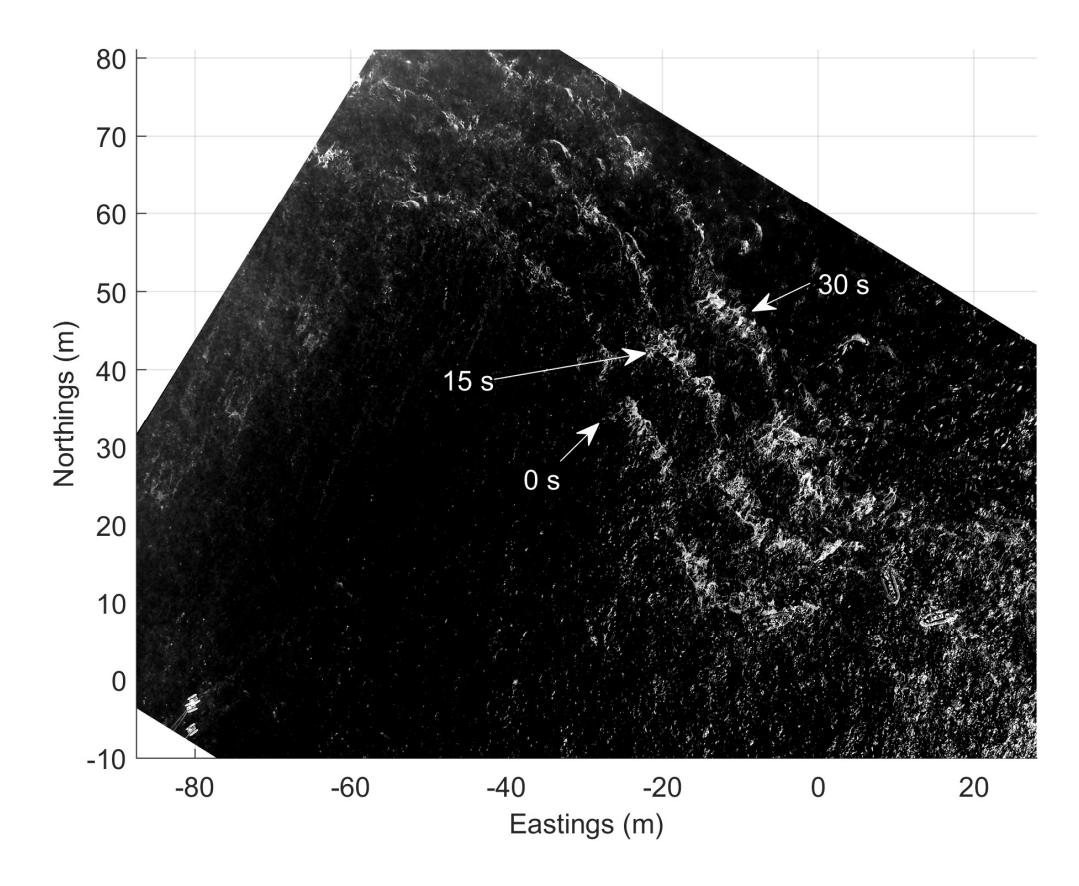


Figure 12: Composite image created from the superimposition of three orthorectified aerial images of the front obtained at three different times, 15 s apart. Image rectification based on the drone GPS data while lens distortion was accounted for using an earlier version of the calibration package of Bouguet (2022).

In another study, Orton and Jay (2005) presented evidence of return flows under the Columbia River tidal pulse (see Fig 2a therein) under upwelling-favorable winds and high river discharge (4,900 m³ s⁻¹). The return flows extended all the way to the bed (~20 m), as is the case in this study. Our observations appear to be in close agreement with those of Solodoch et al. (2020) from the Mississippi River plume. They showed similar return flows under the plume, and they found these to qualitatively resemble the canonical density current structure for a gravity current propagating in stratified waters. As shown in the schematic of Fig. 10, in our case the new front is arriving into already stratified waters (layer 2) qualitative supporting the arguments of Solodoch et al. (2020). The development of such return flows has implications on modeling and representation of tidal plumes and most likely depend not only on river discharge and local water depth but also on the degree of stratification of the ambient waters the plume enters. One important finding of this study is how the shallowing of the base of the plume and the development of the return flows can lead to areas of horizontal flow convergence that can drive the vertical flow divergence shown in the data. Furthermore, these appear to be areas of local maxima in TKE dissipation rates (Fig, 9).

420

425

430

The along-front flow v' observed structure (Fig 6b) of offshore (negative) flow near the surface and onshore directed flow below is attributed to tidal flow. The onshore (positive) directed along-front flow (v') shown in Fig. 6b seems to be explained by the tidal component as predicted using the tidal analysis (Fig. 8c). It is supported by the fact that the pattern is the same for before

and after the arrival of the front. The offshore (negative) directed upper layer flow, most likely, represents the radial spreading of the plume and the influence of the upwelling favorable winds prevailing during this time. Analysis by Papageorgiou (2023) suggested that the vertical structure within the pre-existing plume (layer 1) resembles that of an Ekman layer, suggesting that the movement of the older plume is driven by the wind that is toward the NE (Fig. 2).

4.4 Mixing Processes

435

440

445

450

455

460

465

The density profiles (Fig. 5) from the periods corresponding to groups A to E were matched to corresponding mean velocity profiles (Fig. 6) to estimate the buoyancy frequency (N) and shear (S, where $S^2 = \left(\frac{\partial u}{\partial z}\right)^2 + \left(\frac{\partial v}{\partial z}\right)^2$) for each group. The process included spline interpolation of the flow data (dz = 0.25 m) to the elevations of the buoyancy frequency profiles (dz ~ 0.01 m), and application of a 32-point moving average (~ 0.32 m) prior to estimating gradients. The individual N and S estimates for each profile were then averaged for each group and the profiles are shown in Fig 13 (top). In there the logarithm of the squared shear (4 times) and buoyancy are plotted together on the same plot. These profiles depict an alternative representation of the gradient Richardson number (Ri_g=S²/N²) so that $S^2 > 4N^2$ represents $R_{ig} < 0.25$ suggesting that turbulence can mix the water column (Thorpe, 1987).

In group A, a slightly elevated buoyancy frequency $(4N^2)$ is seen at ~ 2 m depth that reduces slightly at the interface of the pre-existing plume with the ambient waters; then increases again within the ambient waters up to a depth of ~ 6 m and thereafter starts diminishing with increasing water depths. Just before the arrival of the plume (group B), the two maxima described above converge toward the interface of the pre-existing plume and ambient waters. Near the front (group C) high buoyancy frequency values are found near the surface, within the new plume; they slightly diminish inside the pre-existing plume (layer 1) and then increase at the top of the ambient water layer to start diminishing again toward the bed. Immediately after the front's arrival (group D) the elevated buoyancy frequency is maintained up to a depth of 6 m. The near surface values within the new plume are smaller than those seen in group C. Later, behind the front (group E) the maximum buoyancy frequency is observed near the surface with $4N^2$ reaching values of 0.1 s^{-1} . Similar variability is seen in shear with near surface S² values increasing from A to E with maximum near surface shear at A being located at ~ 2 m below the sea surface. Thereafter shear in the upper layer increases with the maximum shifting toward the sea surface attaining its maximum value inside the newly arrived tidal plume at the time corresponding to group E.

Looking at both shear and buoyancy, the ratio of which defines the gradient Richardson number, it is notable that in the lower part of the water column (depths > 6 m, i.e., up to ~5 m above the seabed) squared shear always exceeds $4 \times$ squared buoyancy suggesting Ri_g < 0.25. This holds true for all groups / periods of data collection, before and after the arrival of the front. Near the sea surface the $S^2/4N^2$ ratio tends to oscillate around 1. Prior to the arrival of the plume (A and B) near the surface (< 2 m) there is a tendency for $S^2 > 4N^2$ while farther below and within 2 m of either side of the interface with the ambient waters, buoyancy dominates (i.e., $S^2 < 4N^2$). The latter pattern persists even in group C although its vertical extend is limited to ± 1 m around the interface. Once the front of the new plume arrives (layer 2, group C) buoyancy exceeds shear within the new plume, while shear is higher than buoyance below the interface of layers 1 and 2. Later on (D) both buoyance and shear appear to be balancing each other (i.e., $S^2 \sim 4N^2$) suggesting a gradient Richardson number ~ 0.25 . This balance is maintained within the newly arrived tidal plume (E), but buoyancy seems to be dominant within the pre-existing plume layer (layer 1).

Following Spicer et al (2022) the mixing efficiency parameter Γ was estimated from the CTD data using the parameterization:

$$\Gamma = \frac{R_{if}}{1 - R_{if}} \tag{5}$$

where $Ri_f (= Ri_g Pr_t)$ is the flux Richardson number and Pr_t is the turbulent Prandtl number given by $Pr_t = \sqrt{1 + 4.47Ri_g}$ (Tjernstrom, 1993). As in Spicer et al. (2022) the Ri_f estimates were limited to an upper value of 0.18 resulting in maximum mixing efficiency value of 0.22. The results of these estimates are shown as Γ profiles f Fig. 13 (bottom). In general, maximum mixing efficiency (~0.22) is predicted to be present around the interfaces of the various water layers identified (see shaded areas in figure). This is driven mostly by the upper limit of 0.18 imposed to the Ri_f . In deeper waters (> 6 m) the efficiency parameter drops significantly with some tendency for increase over time from A to E. After the front's arrival, within both the newly arrived and the pre-existing plumes (D and E) Γ = 0.22 suggesting high mixing efficiency presumably because of the high shear present at these times.

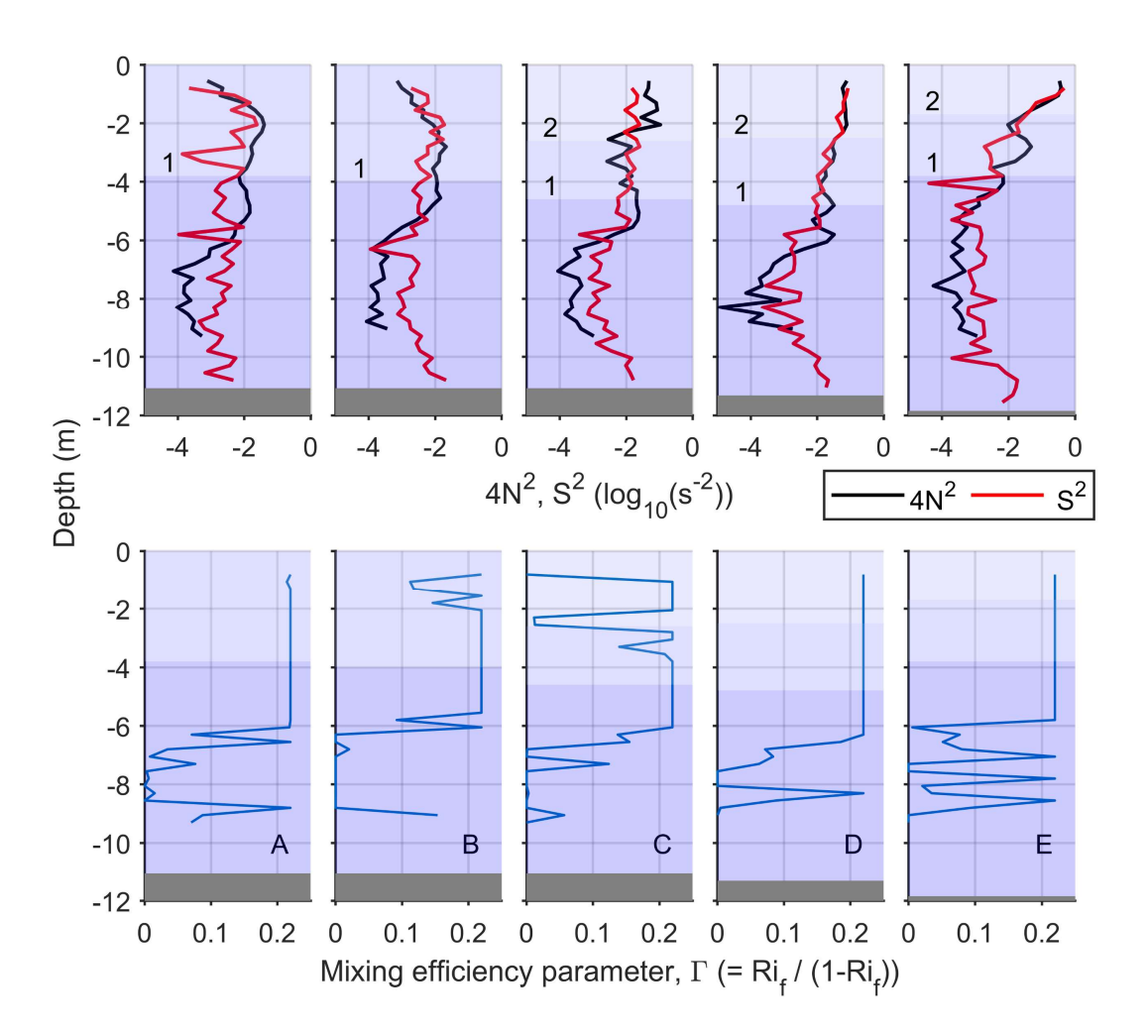


Figure 13: Top: Group (A to E) mean profiles of squared buoyancy frequency $(4 \times N^2)$ and vertical shear (S^2) estimated from the CTD profile shown in Figure 5. $S^2 > 4N^2$ represents $Ri_g < 0.25$ and vice versa. Bottom: Mixing efficiency parameter (Γ) estimates using equation (5). The different shades and numbers 1 and 2 represent the different water masses identified (1 - pre-existing plume, 2 - newly discharged plume).

In summary, using conventional parameterizations of mixing efficiency, it is predicted that maximum mixing occurs near the surface where shear is maximum and diminishes in deeper waters where the water is already well mixed and there is not significant stratification.

480

485

495

500

505

510

In this section mixing processes are examined using the 'available overturn potential energy' (AOPE) in the water column, first presented by Dillon (1982) and later revisited by Smith (2020). The latter work presented an implementation method suitable for profile data with uneven vertical spacing, as is the case for our MicroCTD sensor. The method sorts the density values of the profile and then estimates the relevant Thorpe scales (L_T). Following Smith (2020) the regions of the water column where the cumulative sum of L_T becomes 0 define parts of the water column where overturning occurs (i.e., turbulence patches). The size of each turbulence patch (L_Q) is estimated (see Smith, 2020), and a constant Thorpe scale is assigned to each one of them. Using this method we estimated the dissipation rate (ϵ_p) of turbulence potential energy (TPE) using:

$$\varepsilon_p = \frac{(0.55 + 0.45 \, m/\hat{m})}{\alpha} L_T^2 N_A^3 \tag{6}$$

where $\alpha = 4$, m/\hat{m} is the slope ratio (m-ratio) defined as the slope of a linear fit of the raw data (m) over the slope of a linear fit to the sorted data (\hat{m} , equivalent linear stratification, see Mater et al., 2015), and N_A is the equivalent buoyancy frequency derived from the equivalent linear stratification defined as (Smith, 2020):

$$N_A = \frac{\sqrt[2]{2 \text{ AOPE}}}{L_T} \tag{7}$$

where AOPE is the change in potential energy before and after sorting (see equation (9) in Smith, 2020).

Smith (2020) suggested that the ratio of the Thorpe scale (L_T), representing overturn, over the size of a turbulence patch (L_Q) where the overturn takes place, can provide an insight into the mixing mechanism (i.e., shear-flow vs. density inversion driven). This is called the L-ratio, and it was empirically related to the m-ratio. An m-ratio of -1 represents what Smith (2020) defines as a "young" patch corresponding to conditions of purely buoyancy induced turbulence while a value of +1 represents mixing by pure shear-driven turbulence. Smith (2020) suggested this parameter as a potential indicator of the relevant contribution of the kinetic and potential components in total turbulence energy and dissipation.

The vertical distribution of the Thorpe overturning scales for each one of the profiles, arranged by group, is shown in Fig. 14 (top). These plots appear to be more informative than the $4N^2$ S² plots (Fig. 13) discussed earlier. The larger overturning scales are found near the bed with values ranging from 0.20 to 0.50 m. The smaller (\sim 0.20 m) near bed L_T scales are found at group A, slightly increasing at group B, prior to the arrival of the plume and attaining their largest values (\sim 0.50 m) during and after the arrival of the new plume (groups C to E). Similarly high overturning Thorpe scales are seen near the surface, limited to depths <1.5 m in group A. This layer of high L_T values deepens over time to 2.5 and 4.0 m for group B and C profiles, respectively. After the arrival of the new plume, there are none or very few L_T estimates, as the sorting of the density profiles did not identify any overturns, or the ones estimated were of the order of the vertical resolution of the CTD profiles (\sim 0.01 m) which approach the instrument noise level. In groups A to C no significant overturning is revealed in the region between the surface and bottom layers. The same results are shown in Fig. 14 (middle) where the extent of the regions of overturning (i.e., turbulence patches) are shown.

The slope ratio profiles (Fig. 14, bottom) suggest that the near bed overturning regions, described above, coincide with regions of ratios close to +1 suggesting shear flows being the main driving force. Near the sea surface the slope ratio values show a

scatter from -1 to +1 for group A. The scatter reduces to the range -1 to 0 in group B, suggesting a diminishing contribution of shear flows. This narrow range continues to group C where slopes are between -1 and -0.5. It is worth noting that the areas of highest shear (S^2) shown in Fig. 13 do not coincide with the regions of slope ratio +1 as expected by the Smith (2020) analysis, suggesting that the flow shear is not sufficient to create overturns within the plume.

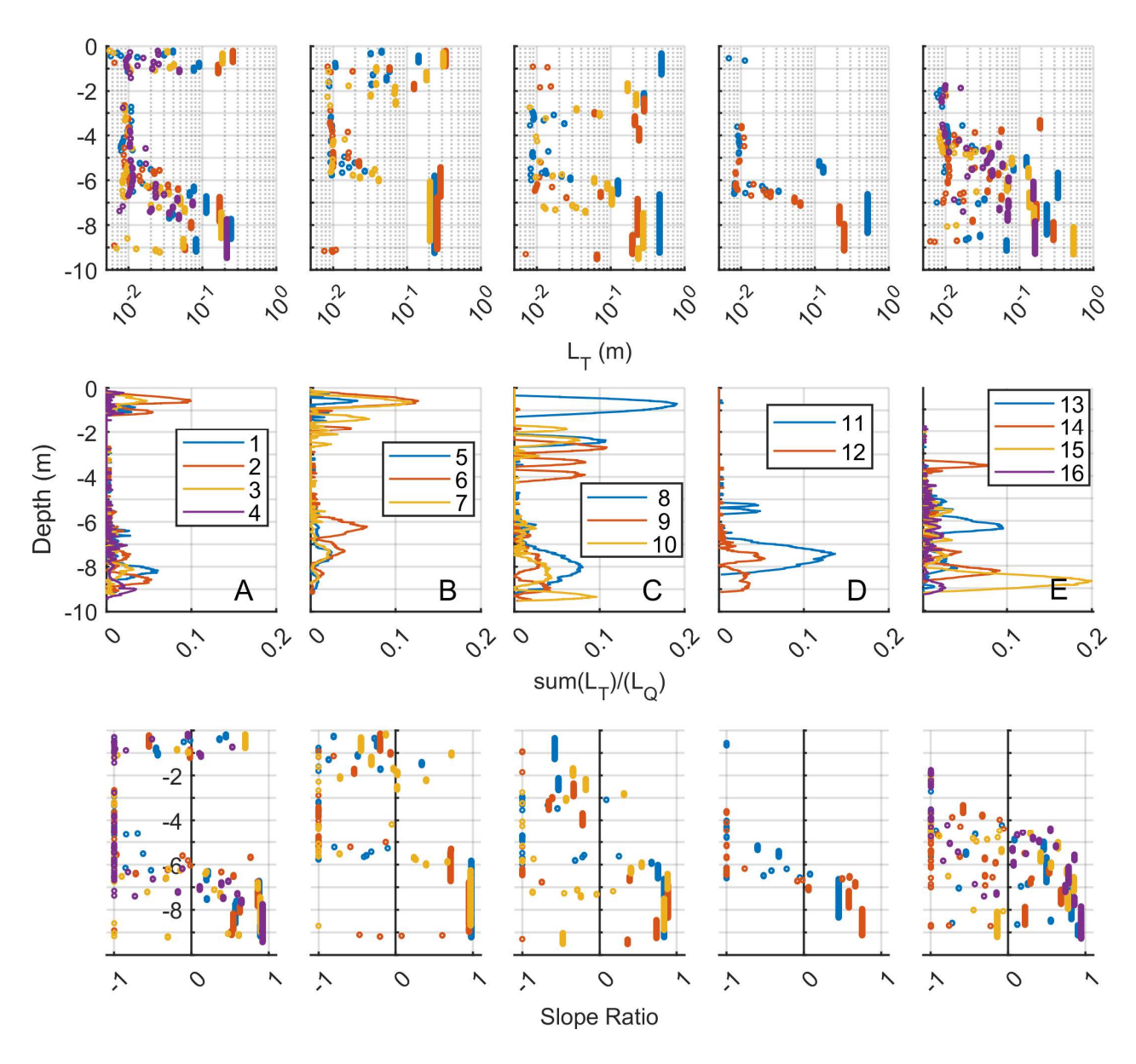


Figure 14: Results of the Smith (2020) method for mixing using the water column turbulent potential energy. Top: Thorpe scales (L_T) estimated from sorting individual density profiles (see Figure 5). Middle: Vertical extend of turbulence patches estimated from summing the estimated Thorpe displacements; the values shown are the sums normalized by the scale (length) of each individual turbulence patch. Bottom: Vertical distribution of the slope ratio indicating the potential mixing mechanism (see text for details). Each column corresponds to a different profile group (A to E) representing different times in relation to the time the plume front passed over the station.

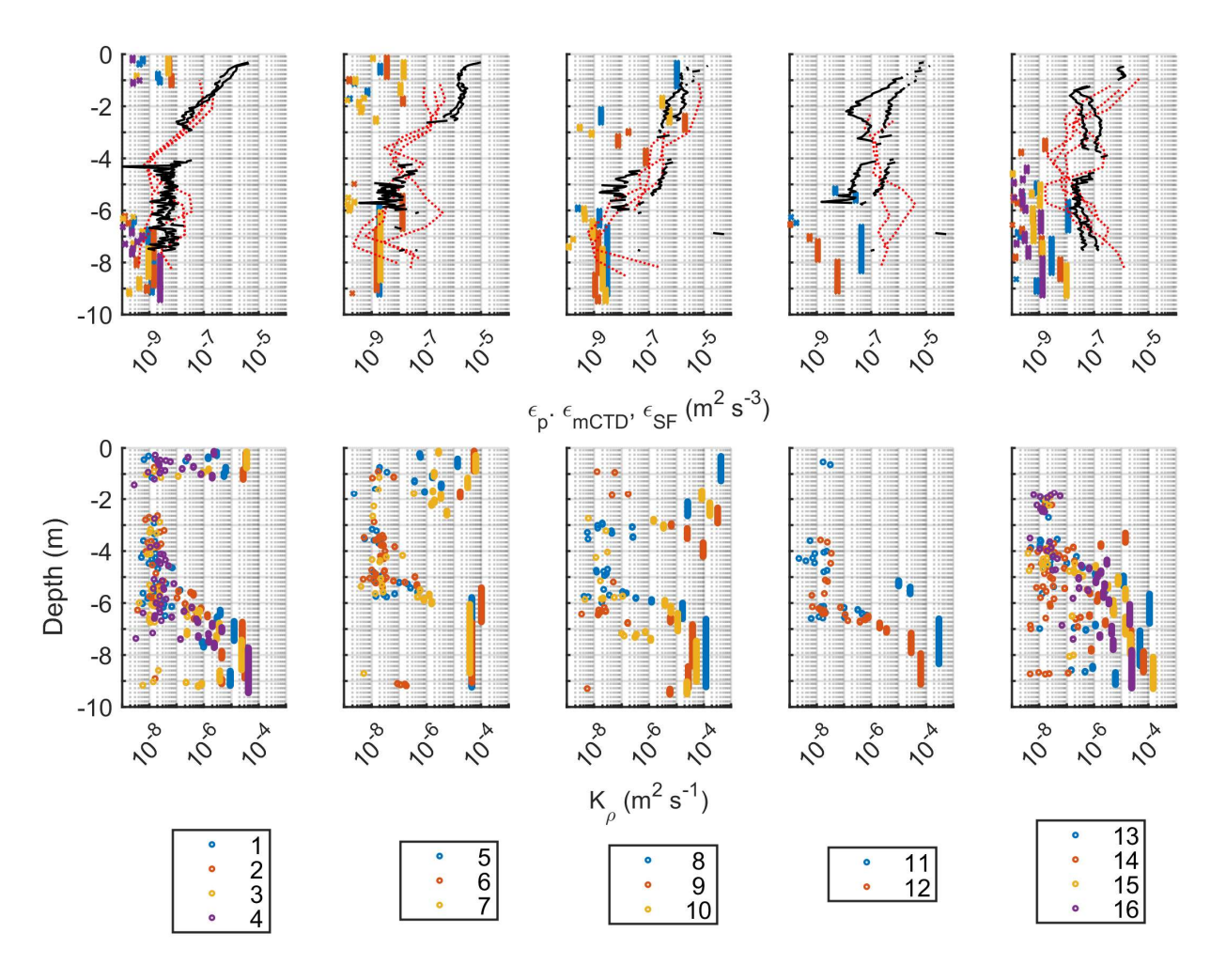


Figure 15: Results of the Smith (2020) method for mixing using the water column turbulent potential energy. Top: Profiles of (i) dissipation rate of turbulent potential energy (ϵ_{ρ}) using the Smith (2020) method (dots); (ii) TKE (ϵ_{k}) from the microstructure (MicroCTD) profiler (red dashed lines) and the AD2CP (black lines) after applying the Structure Function (SF) method (see Figure 9a). Bottom: Density diffusivity (K_{ρ}) estimated using the Smith (2020) method (see text for details). Each column corresponds to a different profile group (A to E) representing different times in relation to the time the plume front passed over the station.

Figure 15 shows the vertical distribution of the estimated TPE dissipation rates (ε_{ρ} , equation 6, Fig. 15 top) and density diffusion coefficient ($K_{\rho} = \varepsilon_{\rho}/N^2$, Fig. 15 bottom). For comparison, the TKE dissipation rate profiles from the AD2CP (SF method, see Fig. 9) and the microstructure on the MicroCTD estimates are also shown on the same figure as black solid and red dotted lines, respectively. Although the plots appear busy, general patterns emerge worth identifying: (i) the TKE dissipation rates (ε_k) from the instantaneous microstructure CTD profiles and the averaged AD2CP HR radial velocities (see section 3.7) show a general qualitative agreement. As discussed earlier and in Papageorgiou (2023) the SF method estimates are time-averaged quantities, while the microstructure estimates are those of individual instantaneous profiles. Nevertheless, all estimates show higher dissipation rates near the sea surface diminishing with depth to $10^{-9} - 10^{-8}$, values close to noise levels. (ii) near the surface in groups A and B profiles, $\varepsilon_{\rho} << \varepsilon_k$, by at least two orders of magnitude, suggesting Γ values \sim 0.01 as suggested by Burchard and Hofmeister (2008). In group C, ε_{ρ} is smaller but similar order as ε_k indicating a higher mixing efficiency than in A and B. (iii) Near the bed, in the regions where the slope ratio was found to be \sim +1, the TKE and TPE dissipation rates appear to be of the

520

same order, making the argument of a mixing efficiency coefficient (Γ) with values between 0.2 and 1 plausible. (iv) Within the new plume, although relatively high TKE dissipation rates are estimated by both the SF method and the microstructure probe, the overturning analysis suggests no vertical mixing. This discrepancy within the new plume could potentially be attributed to local anisotropic turbulence (Lewin and Caulfield, 2024) that does not contribute to vertical mixing and / or turbulence advection that we have not estimates of. The high velocity shear found inside the new plume suggests that straining could be a potential mechanism for maintaining the observed stratification inside the plume, which to our knowledge has not been assessed for plume interiors.

530

535

540

545

550

In summary, the vertically integrated layer estimates of TKE and TPE dissipation rates, along with density diffusivity, are listed in Table for the different groups / times before (A, B), during (C) and after (D, E) the passage of the front.

Table 3. Layer integrated estimates of dissipation rate of TKE (ϵ_k), turbulent potential energy (ϵ_p), and density diffusivity (K_ρ) for the different regions before (A, B), at (C), and after (D, E) the plume front passage. The mixing efficiency parameter Γ estimated for the corresponding dissipation rates is also listed.

		A	В	С	D	Е
$\varepsilon_k (\mathrm{m^2 s^{-3}})$	Layer 2	-	-	1.28x10 ⁻⁶	2.19x10 ⁻⁶	2.27x10 ⁻⁶
	Layer 1	6.88x10 ⁻⁷	8.05x10 ⁻⁷	9.51x10 ⁻⁷	9.72x10 ⁻⁷	3.74x10 ⁻⁷
	Ambient	1.33x10 ⁻⁸	4.25x10 ⁻⁹	3.93x10 ⁻⁹	1.27x10 ⁻⁸	2.07x10 ⁻⁷
$\varepsilon_p (\mathrm{m^2 s^{-3}})$	Layer 2	-	-	5.94 x 10 ⁻⁸	9.15 x 10 ⁻¹⁴	~0
	Layer 1	4.93 x 10 ⁻¹⁰	8.64 x 10 ⁻⁹	5.59 x 10 ⁻¹¹	2.81 x 10 ⁻¹³	4.49 x 10 ⁻¹²
	Ambient	5.09 x 10 ⁻¹⁰	1.29 x 10 ⁻⁹	1.44 x 10 ⁻⁹	1.20 x 10 ⁻⁸	1.56 x 10 ⁻⁹
$K_{ ho} ({ m m}^2 { m s}^{-1})$	Layer 2	-	-	1.75 x 10 ⁻⁵	1.78 x 10 ⁻¹⁰	0
	Layer 1	3.09 x 10 ⁻⁶	6.35 x 10 ⁻⁶	7.84 x 10 ⁻⁷	8.08 x 10 ⁻¹⁰	3.82 x 10 ⁻⁸
	Ambient	1.02 x 10 ⁻⁵	2.30 x 10 ⁻⁵	2.62 x 10 ⁻⁵	8.30 x 10 ⁻⁵	2.24 x 10 ⁻⁵
$\Gamma = \varepsilon_p / \varepsilon_k$	Layer 2	-	-	0.05	< 0.01	< 0.01
	Layer 1	< 0.01	0.01	< 0.01	< 0.01	< 0.01
	Ambient	0.04	0.30	0.37	0.95	0.01

It is notable that within the plume (layer 2), density diffusivity is highest ($\sim 10^{-5}$ m² s⁻¹) during the passage of the front (group C) and quickly reduces to $\sim 10^{-10}$ m² s⁻¹ soon after (group D) to diminishing some 1-2 hours later (group E). This suggests vertical mixing is shut down behind the front despite the highly sheared flows occurring there (see Fig. 9c). The gradient Richardson number within the plume (layer 2, see Fig 13 top) is ~ 0.25 with corresponding squared buoyancy frequency (N²) values of 0.02 and 0.08 s⁻¹, for D and E, respectively. Using these values with the corresponding TKE dissipation rates listed in Table 3 we derive buoyancy Reynolds numbers (Re_b) of the order of 8 and 2 for C and D, respectively. Imberger (1983, cited in Delatolas et al, 2023) suggested that when Re_b < 21 turbulence ceases to be isotropic as stratification suppresses vertical mixing. However, in their studies ϵ_k was of the of 10⁻⁶ near the front and reduced to 10⁻⁸ although our results indicate a higher, almost constant dissipation rate of 10⁻⁶ within the tidal plume. Our diffusivity estimates behind the plume (C and D) appear to be even lower than those presented in Ivey et al., (2020) for Re_b ~ 10 (see their Fig. 3) and high gradient Richardson numbers, for a pure convective mixing. Near the bed and within the ambient water layer the TKE dissipation rate is extremely low (10⁻⁸ to 10⁻⁹ m² s⁻³) increasing

to 10^{-7} m² s⁻³ at E. This is attributed to bottom boundary layer turbulence and increased tidal velocities over time as shown in Fig. 8c. Near bed density diffusivity appears to remain constant ~3x10⁻⁵ m² s⁻¹. In terms of mixing efficiency, mixing is more efficient in the bottom boundary layer with Γ values ranging from 0.01 to 1.

5. Conclusions and Summary

555

560

565

570

575

580

585

This study presented comprehensive observational data highlighting the kinematics and mixing processes within a tidal river plume and its interaction with a pre-existing plume and the ambient waters. Flow and mixing processes some 2 hours before and after the passage of a front at a location with a total depth of 11.5 m were analyzed. Prior to the arrival of the new plume, a pre-existing plume extending some 4 m below the sea surface was present. The water density of the pre-existing front was 1,023.6 kg m⁻³ while the underlaying ambient waters had a density of 1,024.8 kg/m³. The water density of the newly arrived front was 1,020.7 kg/m³ and its depth was 2.6 m, diminishing over time mainly due to radial spreading.

The relative propagation speed of the front associated with the newly discharged plume was 0.36 m/s while behind the front the propagation speed was 0.40 m/s. A frontal Froude number of 1.32 was estimated suggesting that the new plume was propagating as a gravity current entering already stratified coastal waters

The velocity field showed an estuarine-like circulation in the direction of front propagation with a counteracting flow under the plume. A strong divergence in the across-front velocity evolving into shallower depth over time seems to drive upward and downward vertical velocities of a few cm s⁻¹. In the along front direction, a similar two-layer upwelling-like counteracting flow structure was observed but its pattern is consistent for both periods before and after the arrival of the plume. The only effect of the plume arrival is the enhancement of the offshore flow under it. This lower layer flow seems to be closely related to the ambient tidal currents in the area while the top layer is likely influenced mainly by wind forcing.

Our estimates of TKE dissipation rates are like those of Delatolas et al. (2023) and other studies that documented enhanced dissipation at river plume fronts and a sharp decline in turbulence within the stratified plume interior, reinforcing the idea that frontal regions are hotspots of mixing. We also observe sustained local dissipation maxima near the plume base associated with the depths of enhanced shear associated with the reversed flow; however, this is not matched by similarly high mixing efficiency, suggesting suppressed mixing despite active shear.

Tidally induced bottom boundary mixing is present and efficient but does not seem to influence mixing within the plume itself. Given the microtidal regime of our study site, tidal mixing was limited to the benthic boundary layer and did not seem to affect the mixing within the plume as was observed by Spicer et al (2021) for the Connecticut River plume.

Our comparison of mixing processes using a common parameterization based on gradient Richardson gradient number and the available overturn potential energy in the water column, as presented by Smith (2020) did not agree. The two methods provided contradictory results with the parameterization suggesting higher mixing efficiency within the plume, while the overturn potential analysis revealed that mixing occurred mainly in the bottom boundary layer. Near the sea surface, prior to the arrival of the new plume mixing was dominated by a mixture of overturning and wind-induced shear flows. However, within the gravity current, and further from the frontal area, the mixing efficiency of the shear-induced turbulence was very small, despite the high TKE dissipation rates measured in that region. This observation together with the observations of the counteracting flows under the plume raises the question of the potential effect of straining as a stabilizing force. River plume studies have been focusing on the

role of advection in plume movement and evolution without including the effects of straining. de Boer et al. (2008) have argued that both mechanisms need to be included as the latter affects stratification. In their study, deBoer et al (2006) showed the reestablishment in stratification on the Rhine plume during neap tides because of straining that led to the development of counteracting surface and bottom currents during this period (neap tides). During spring tides, mixing was enhanced and no stratification was present while the currents were uniform in the water column. The development of the observed countercurrent along the plume direction in this study and the reduced mixing revealed by the TPE analysis suggest that straining might be an important process to include in the study of smaller plumes like the one encountered in this study.

Data Availability

590

595

605

610

615

The data presented in this manuscript are available as MATLAB (*.mat) files (Papageorgiou et al., 2025). For a description and access visit Zenodo (https://doi.org/10.5281/zenodo.14687082).

Code Availability

The data were analyzed using standard analyses techniques implemented in MATLAB and modifications of the codes listed below.

The Structure Function analysis was carried out using the Zeiden et al. (2023) method and their codes are publicly available at https://github.com/SASlabgroup/SWIFT-codes.

The Smith (2020) analysis for mixing using the water column turbulent potential energy was done using a modified version of the MATLAB software code published in Smith (2020) online supplemental materials available at https://journals.ametsoc.org/view/journals/atot/37/1/jtech-d-18-0234.1.xml? tab body=supplementary-materials.

Author Contributions

GV, AY and DF conceived the study, designed the experiments and participated in data collection. GV and CP did the data processing and analysis and wrote the manuscript with contributions from all co-authors. AY and DF handled the data processing for the microstructure and microCTD instrument. GV and CP developed the RoboCat and thermistor array system used in this study. GV, AY and DF acquired funding and managed the project. All authors reviewed and edited the draft version.

Competing interests

The authors declare that they have no conflicts of interest.

Acknowledgments

The authors would like to thank the captain and crew of the R/V *Savannah* for their dedication and help during the data collection period. Some of the technology developed for this project would have not been possible without the help Dr. D. Cahl and Mr. M.C. Wescott. Dr. Cahl also assisted in data collection as did several undergraduate and graduate students from the University

of South Carolina and Coastal Carolina University. This material is based upon work supported by the U.S. National Science Foundation (NSF) under Grant Nos 2148479 and 2148480. George Voulgaris' contribution was partially carried out while at NSF as part of his approved Independent Research/Development (IR/D) plan. Any opinions, findings, and conclusions expressed in this material are those of the authors and do not necessarily reflect the views of the NSF.

References

620

630

- Arneborg, L., Fiekas, V., Umlauf, L., and Burchard, H.: Gravity Current Dynamics and Entrainment—A Process Study Based on Observations in the Arkona Basin. J. Phys. Oceanogr., 37, 2094–2113, https://doi.org/10.1175/JPO3110.1, 2007.
- Bouguet, J.-Y.: Camera calibration toolbox for Matlab (1.0). CaltechDATA. https://doi.org/10.22002/D1.20164, 2022. Britter, R. E., & Simpson, J. E. (1978). Experiments on the dynamics of a gravity current head. *Journal of Fluid Mechanics*, 88(2), 223-240.
 - Burchard, H and Hofmeister, R.: A dynamic equation for the potential energy anomaly for analysing mixing and stratification in estuaries and coastal seas, Estuarine, Coastal and Shelf Science, 77(4): 679-687, https://doi.org/10.1016/j.ecss.2007.10.025, 2008.
 - de Boer, G. J., Pietrzak, J. D., and Winterwerp, J. C.: On the vertical structure of the Rhine region of freshwater influence. Ocean Dyn., 56, 198–216, https://doi.org/10.1007/s10236-005-0042-1, 2006.
 - de Boer, G. J., Pietrzak, J. D., and Winterwerp, J. C.: Using the potential energy anomaly equation to investigate tidal straining and advection of stratification in a region of freshwater influence. Ocean Modell., 22, 1–11,
- 635 https://doi.org/10.1016/j.ocemod.2007.12.003., 2008.
 - Delatolas, N., MacDonald, D. G., Goodman, L., Whitney, M., Huguenard K., and Cole. K.: Comparison of structure and turbulent mixing between lateral and leading-edge river plume fronts: microstructure observations from a T-REMUS AUV. Estuarine, Coastal and Shelf Science, 283,108234, https://doi.org/10.1016/j.ecss.2023.108234, 2023.
- Dillon T. M.: Vertical overturns: A comparison of Thorpe and Ozmidov length scales. J. Geophys. Res., 87, 9601-9613, https://doi.org/10.1029/JC087iC12p09601, 1982.
 - Edson, J. B., Raju, J. V. S., Weller, R. A., Bigorre, S., Plueddemann, A., Fairall, C. W., Miller, S., Mahrt, L., Vickers, D. and Hersbach, H.: On the Exchange of momentum over the open ocean. J. Phys. Oceanogr., 43, 1589–1610. http://dx.doi.org/10.1175/JPO-D-12-0173.1, 2013.
- Fairall, C. W., Bradley, E. F., Hare, J. E., Grachev, A. A., and Edson, J. B.: Bulk Parameterization of Air–Sea Fluxes: Updates and Verification for the COARE Algorithm. J. Climate, 16, 571–591, <a href="https://doi.org/10.1175/1520-0442(2003)016<0571:BPOASF>2.0.CO;2">https://doi.org/10.1175/1520-0442(2003)016<0571:BPOASF>2.0.CO;2, 2003.
 - Fong, D. A., and Geyer, W. R: The Alongshore Transport of Freshwater in a Surface-Trapped River Plume. J. Phys. Oceanogr., 32, 957–972, https://doi.org/10.1175/1520-0485(2002)032<0957:TATOFI>2.0.CO;2, 2002.
 - Garvine, R. W.: Radial spreading of buoyant, surface plumes in coastal waters, J. Geophys. Res., 89(C2), 1989–1996, doi:10.1029/JC089iC02p01989, 1984.

- Hetland, R. D.: The effects of mixing and spreading on density in near-field river plumes. Dynamics of Atmospheres and Oceans, 49(1), 37-53, https://doi.org/10.1016/j.dynatmoce.2008.11.003, 2010.
- Horner-Devine, A. R., Chickadel, C. C. and MacDonald, D. G.: Coherent Structures and Mixing at a River Plume Front. In Coherent Flow Structures at Earth's Surface (eds J.G. Venditti, J.L. Best, M. Church and R.J. Hardy).
- 655 https://doi.org/10.1002/9781118527221.ch23, 2013.
 - Horner-Devine, A. R., Jay, D. A., Orton, P. M., and Spahn, E. Y.: A conceptual model of the strongly tidal Columbia River plume, Journal of Marine Systems, 78 (3), 460-475, https://doi.org/10.1016/j.jmarsys.2008.11.025, 2009
 - Horner-Devine, A. R., Hetland, R. D., and MacDonald, D. G.: Mixing and transport in coastal river plumes. Annual Review of Fluid Mechanics, 47, 569-594, https://doi.org/10.1146/annurev-fluid-010313-141408, 2015.
- Huppert H. E. and Simpson J. E.: The slumping of gravity currents. Journal of Fluid Mechanics 99(4): 785-799. doi:10.1017/S0022112080000894, 1980.
 - Imberger, J.: Tidal Jet Frontogenesis. Transactions of the Institution of Engineers, Australia. Mechanical Engineering, ME8, 4, 171 180, 1983.
- Ivey, G.N., Bluteau, C.E., Gayen, B., Jones, N.L., and Sohail, T.: Roles of shear and convection in driving mixing in the ocean.

 Geophysical Research Letters, 48, e2020GL089455, https://doi.org/10.1029/2020GL089455, 2020.
 - Kastner, S. E. Horner-Devine, A. R., and Thomson, J.: The influence of wind and waves on spreading and mixing in the Fraser River plume. J. Geophys. Res., 123, 6818–6840, https://doi.org/10.1029/2018JC013765, 2018.
 - Kay, D. J., and Jay D. A.: Interfacial mixing in a highly stratified estuary 1. Characteristics of mixing, J. Geophys. Res., 108, 3072, doi:10.1029/2000JC000252, C3, 2003.
- Kilcher, L. F., Nash, J. D., and Moum, J. N.: The role of turbulence stress divergence in decelerating a river plume. J. Geophys. Res., 117, C05032, doi:10.1029/2011JC007398, 2012.
 - Kim, Y. H., and Voulgaris, G.: Effect of channel bifurcation on residual estuarine circulation: Winyah Bay, South Carolina. Estuarine, Coastal and Shelf Science, 65(4), 671-686, https://doi.org/10.1016/j.ecss.2005.07.004, 2005.
- Lavey, A. C., Geyer, W. R., Scully, M. E.: Broadband acoustic quantification of stratified turbulence. J. Acoust. Soc. Am. 2013

 Jul;134(1):40-54. doi: 10.1121/1.4807780, 2013.
 - Lewin SF, Caulfield CP. Evidence for layered anisotropic stratified turbulence in a freely evolving horizontal shear flow. Journal of Fluid Mechanics, 983:A20, doi:10.1017/jfm.2024.121, 2024.
 - Li, C., Nels on, J. R., and Koziana, J. V.: Cross-shelf passage of coastal water transport at the South Atlantic Bight observed with MODIS Ocean Color/SST. Geophys. Res. Lett., 30,1257, doi:10.1029/2002GL016496, 2003.
- Luketina, D.A., and Imberger, J.: Characteristics of a Surface Buoyant Jet. J. Geophys. Res., 92(C5), 5435-5447, doi: 10.1029/JC092iC05p05435, 1987.
 - Mater, B. D. and Venayagamoorthy, S. K.: The quest for an unambiguous parameterization of mixing efficiency in stably stratified geophysical flows, Geophys. Res. Lett., 41, 4646–4653, doi:10.1002/2014GL060571, 2014.

- Mater, B. D., Venayagamoorthy, S. K., St Laurent, L., and Moum, J. N.: Biases in Thorpe-scale estimates of turbulence dissipation. Part I: Assessments from large-scale overturns in oceanographic data. J. Phys. Oceanogr., 45, 2497–2521, https://doi.org/10.1175/JPO-D-14-0128.1, 2015.
 - MacDonald, D. G., and Geyer W. R., Turbulent energy production and entrainment at a highly stratified estuarine front, J. Geophys. Res., 109, C05004, doi:10.1029/2003JC002094., 2004.
- MacDonald, D. G., Goodman, L., and Hetland, R. D.: Turbulent dissipation in a near-field river plume: A comparison of control volume and microstructure observations with a numerical model. J. Geophys. Res., 112, C07026, doi:10.1029/2006JC004075, 2007.
 - Marmorino, G. O., and Trump, C. L., Gravity current structure of the Chesapeake Bay outflow plume, J. Geophys. Res., 105(C12), 28847–28861, doi:10.1029/2000JC000225, 2000.
 - Münchow, A., and Garvine, R.W.: Buoyancy and wind forcing of a coastal current. J. Mar. Res, 51, 293–322, https://doi.org/10.1357/0022240933223747, 1993.

695

- O'Donnell, J., Ackleson, S. G., and Levine, E. R.: On the spatial scales of a river plume. J. Geophys. Res., 113, C04017, doi: 10.1029/2007JC004440, 2008.
- Orton, P. M., and Jay, D. A.: Observations at the tidal plume front of a high-volume river outflow. Geophys. Res. Lett., 32, L11605, doi:10.1029/2005GL022372, 2005.
- Osborn, T. R.: Estimates of the Local Rate of Vertical Diffusion from Dissipation Measurements. J. Phys. Oceanogr., 10, 83–89, https://doi.org/10.1175/1520-0485(1980)010<0083:EOTLRO>2.0.CO;2. 1980.
 - Papageorgiou, C. T.: Robocat: An autonomous surface vehicle (ASV) for near-surface hydrodynamic measurements in buoyant plumes. Development and case study. Master's thesis, University of South Carolina, Columbia, SC, USA. Retrieved from https://scholarcommons.sc.edu/etd/7640, 2023.
- Papageorgiou, C., Voulgaris, G., Yankovsky, A., and Fribance, D.: Dataset for Manuscript: "Flow Structure and Mixing Near a Small River Plume Front: Winyah Bay, SC, USA" [Data set]. In Ocean Sci. Zenodo. https://doi.org/10.5281/zenodo.14687082, 2025.
 - Patchineelam S.M.: Fine-grained sediment dynamics and budget: Winyah Bay estuary, South Carolina. Unpublished Ph.D. Dissertation, University of South Carolina, 1999.
- Peters, H.: Spatial and temporal variability of turbulent mixing in an estuary. Journal of Marine Research, 57, 805–845, 1999

 Pritchard, M., and D. A. Huntley: A simplified energy and mixing budget for a small river plume discharge, *J. Geophys.*Res., 111, C03019, doi:10.1029/2005JC002984, 2006.
 - Scannell, B. D., Rippeth, T. P., Simpson, J. H., Polton, J. A., and Hopkins, J. E.: Correcting surface wave bias in structure function estimates of turbulent kinetic energy dissipation rate. J. Atmos. Oceanic Technol., 34, 2257–2273, https://doi.org/10.1175/JTECH-D-17-0059.1, 2017.
 - Scotti, A.: Biases in Thorpe-scale estimates of turbulence dissipation. Part II: Energetics arguments and turbulence simulations. J. Phys. Oceanogr., 45, 2522–2543, https://doi.org/10.1175/JPO-D-14-0092.1, 2015.

- Simpson, J. H.: The shelf-sea fronts: implications of their existence and behaviour. Philosophical Transactions of the Royal Society London Series A, 302, pp. 531-546, 1981.
- Simpson, J. E. and Britter, R. E.: The dynamics of the head of a gravity current advancing over a horizontal surface. Journal of Fluid Mechanics, 94(3), 477–495. doi:10.1017/S0022112079001142, 1979.
 - Simpson, J. E. and Britter, R. E.: A laboratory model of an atmospheric meso-front. Q.J.R. Meteorol. Soc., 106: 485-500. https://doi.org/10.1002/qj.49710644907, 1980.
- Simpson, J.H., Brown, J., Matthews, J., Allen, G.: Tidal straining, density currents, and stirring in the control of estuarine stratification. Estuaries, 26, 1579-1590, 1990.
 - Smith, J. A.: A comparison of two methods using Thorpe sorting to estimated mixing. J. Atmos. Oceanic Technol., 37, 3-15, https://doi.org/10.1175/JTECH-D-18-0234.1, 2020.
 - Solodoch, A., Molemaker, J.M, Srinivasan, K., Berta, M., Marie, L., and Jagannathan, A.: Observations of shoaling density current regime changes in internal wave interactions. J. Phys. Oceanogr., 50, 1733–1751, https://doi.org/10.1175/JPO-D-19-0176.1, 2020.
 - Spicer, P., Huguenard, K., Cole, K. L., MacDonald, D. G., and Whitney, M. M. Evolving interior mixing regimes in a tidal river plume. *Geophysical Research Letters*, 49, e2022GL099633. https://doi.org/10.1029/2022GL099633, 2022
 - Spicer, P., Cole, K. L., Huguenard, K., MacDonald, D. G. and Whitney, M.M.: The effect of bottom-generated tidal mixing on tidally pulsed river plumes. *J. Phys. Oceanogr.*, **51**, 2223–2241, https://doi.org/10.1175/JPO-D-20-0228.1, 2021
- Tjernstrom, M. Turbulence length scales in stably stratified free shear flow analyzed from slant aircraft profiles. *J. Appl. Meteor.*, 32, 948–963. https://doi.org/10.1175/1520-0450(1993)032<0948:tlsiss>2.0.co;2, 1993.
 - Thomson, J., Nylund, S., Moulton, M., de Klerk, A., Talbert, J., Guerra, M., Kastner, S.E., Smith, M.M., Schwendeman, M., & Zippel, S.F.: A new version of the SWIFT platform for waves, currents, and turbulence in the ocean surface layer. *2019* IEEE/OES Twelfth Current, Waves and Turbulence Measurement (CWTM), 1-7., 2019.
- Thorpe, S. A.: Transitional phenomena and the development of turbulence in stratified fluids: A review. J. Geophys. Res., 92(C5), 5231. https://doi.org/10.1029/JC092iC05p05231, 1987
 - von Karman, T.: The engineer grapples with nonlinear problems. Bull. Amer. Math. Soc., 46, 615–683, 1940.
 - Yankovsky, A.E., Fribance, D.B., Cahl, D., and Voulgaris, G.: Offshore Spreading of a Supercritical Plume Under Upwelling Wind Forcing: A Case Study of the Winyah Bay Outflow. Front. Mar. Sci. 8:785967.
- 745 <u>https://doi.org/10.3389/fmars.2021.785967</u>, 2022.

- Whitney, M. M., Spicer, P., MacDonald, D. G., Huguenard, K. D., Cole, K. L., Jia, Y., and Delatolas, N.: Mixing of the Connecticut River plume during ambient flood tides: Spatial heterogeneity and contributions of bottom-generated and interfacial mixing. J. Geophys. Res., Oceans, 129, e2023JC020423. https://doi.org/10.1029/2023JC020423, 2024.
- Wiles, P. J., Rippeth, T. P., Simpson, J. H., and Hendricks, P. J. (2006). A novel technique for measuring the rate of turbulent dissipation in the marine environment. *Geophysical Research Letters*, *33*(21).

Zeiden, K., Thomson, J., and Girton, J.: Estimating profiles of dissipation rate in the upper ocean using acoustic Doppler measurements made from surface-following platforms. J. Atmos. Oceanic Technol., 40(12), 1571-1589. https://doi.org/10.1175/JTECH-D-23-0027.1, 2023.

Zippel, S. F., Thomson J., and Farquharson, G.: Turbulence from breaking surface waves at a river mouth. J. Phys. Oceanogr., 48, 435–453, https://doi.org/10.1175/JPO-D-17-0122.1, 2018.

APPENDIX A

765

The plume depth was quantitatively estimated using the generalized equation of Arneborg et al. (2007), which was originally developed to estimate the thickness (D) of a bottom gravity current:

760
$$D = \frac{2 \int_{-h}^{0} \frac{\rho(z) - \rho_0}{\rho_0} z \, dz}{\int_{-h}^{0} \frac{\rho(z) - \rho_0}{\rho_0} \, dz}$$
A.1

where, z is the elevation below sea surface, h is the total depth of the water column, $\rho(z)$ is the density at elevation z and ρ_0 is the reference ambient density (1,024.8 kg/m³ in this study).

Given our observations that a two-layer structure is developed into a three-layer structure we modified equation (3) so that we can track the depth of the pre-existing (D₁) and the new (D₂) plume reflecting the system's state both before $(t < t_f)$ and after $(t > t_f)$ the front's arrival at time t_f . The modified equations are:

$$D_{1}(t) = \frac{2 \int_{-h}^{0} \frac{\rho(z,t) - \rho_{0}}{\rho_{0}} z \, dz}{\int_{-h}^{0} \frac{\rho(z,t) - \rho_{0}}{\rho_{0}} \, dz}, \text{ for } t < t_{f}$$

$$A.2$$

$$D_2(t) = 0$$
, for $t < t_f$

$$D_2(t) = \frac{2\int_{-\langle D_1(t < t_f) \rangle}^{0} \frac{\rho(z,t) - \rho(-D_1,t)}{\rho(-D_1,t)} \frac{z}{z} dz}{\int_{-\langle D_1(t < t_f) \rangle}^{0} \frac{\rho(z,t) - \rho(-D_1,t)}{\rho(-D_1,t)} dz}, \quad t \ge t_f$$

$$A.4$$